Si, CdTe and CdZnTe radiation detectors for imaging applications

Tom Schulman

University of Helsinki, Finland

Dissertation for the degree of Doctor of Philosophy to be presented with due permission for public examination and debate in auditorium Physicum E204 at the Faculty of Science of the University of Helsinki, Finland on the 19th of June 2006 at 12 o'clock noon.

ISBN 952-92-0428-0
Yliopistopaino 2006, Helsinki, Finland

Contents

Acknowledgements

Summary of publications

Contribution of the author to the publications

1. Introduction

2. Silicon strip detectors

3. Digital X- and gamma ray imaging
   3.1 Direct and indirect conversion of X- and gamma ray energy
   3.2 Photon counting and charge integration imaging modes
   3.3 Large area imaging

4. Charge integrating silicon pixel detectors
   4.1 Detector design
   4.2 Bump bonding and sensor module structure
   4.3 Front end CMOS circuitry and signal readout
   4.4 Calibration and image acquisition
   4.5 Application to dental intra oral X-ray imaging

5. CdTe and CdZnTe pixel detectors
   5.1 Material properties
   5.2 Pixelisation process
   5.3 Bump bonding
   5.4 Detector and sensor module design and tiling techniques
   5.5 Front end CMOS circuitry
   5.6 Application to real time and dental panoramic X-ray imaging
   5.7 Gamma imaging

6. Performance analysis
   6.1 Definitions and methods
   6.2 Performance of the silicon intra oral imaging sensor
   6.3 Performance of the CdTe real time imager
   6.4 Simulated photo peak efficiency of CdTe and CdZnTe gamma cameras
      6.4.1 Physical model
      6.4.2 Simulation results

7. Radiation hardness issues
   7.1 Dose determination
   7.2 CMOS electronics
   7.3 Silicon detectors
   7.4 CdTe and CdZnTe detectors

8. Conclusions

References

Acknowledgements

Most sincerely and highly I acknowledge the support of **Prof. Risto Orava** to my career as a detector physicist from the very beginning back in 1989 until today. Amazingly enough, he never lost his hope in me, not even during the years of my strange adventures in the Middle East. I consider him a great visionary and the truly grand old man (though not that old yet) in the short history of the Finnish detector research and development.

Equally highly I express my gratefulness to **Dr. Konstantinos Spartiotis**, the founder of Oy Simage Ltd. and Oy Ajat Ltd. and the true pioneer in creating the impossible in crystalline semiconductor detector technology. His commitment and zeal to push forward the limits of technology (and his engineers) are absolutely amazing.

I have been granted the privilege to work together with some exquisite genius. I would like to thank especially **Jouni Pyyhtiä**, a fine friend and the most brilliant expert in electronics design in the whole of the known universe. His contribution to the technology described in this work is far greater than my own.

I am in debt also to my colleagues at Ajat, **Joonas Havulinna**, **Jussi Kinnari**, **Pasi Laukka**, **Anssi Leppänen**, **Kari Muukkonen**, **Olli Männistö**, **Tuomas Pantsar**, **Tero Pesu** and **Kimmo Puhakka**. I thank also **Markku Eräluoto** and **Jari Kosonen** for the great time at Simage.

I deeply acknowledge the contribution of **Dr. Panu Jalas** who in the very beginning of our visions of conquering the world with a new imaging technology boldly introduced us to the challenging material of CdZnTe.

I thank **Jouni Heino**, **Kari Kurvinen**, **Dr. Mikko Laakso**, **Rauno Lauhakangas** and **Antti Numminen** for the good old days and games with strip detectors.

I sincerely would like to thank also **Prof. Dr. Yücel Aşkın**, the rector of the YYÜ University in Van, Eastern Turkey, who granted me the most exciting opportunity to teach physics to the Turkish and Kurdish youth. I am also very grateful to my colleagues at the Physics Department of the YYÜ University. *Aranızda kardeş gibi beni kabul ettiğiniz için hepinize derin derin teşekkür ederim!*

Finally I want to thank my dear wife **Marjatta** and all of my five fantastic children. Compared to all the adventures we have experienced together this thesis is “like a drop in a bucket, and is regarded as a speck of dust on a balance”. No words can describe my feelings of gratitude to our loving God for the treasure I own in you Marjatta.

11th of May 2006, Espoo, Finland

Tom Schulman

Summary of Publications

I R. Brenner, I. Hietanen, J. Lindgren, R. Orava, C. Rönnqvist, T. Schulman, T. Tuuva and M. Voutilainen, *Double-sided capacitively coupled silicon strip detectors on a 100 mm wafer*, NIM A 315, 1992.

II R. Lauhakangas, P. Laurikainen, R. Orava, R. Ostonen, J. Pyyhtiä, T. Schulman, K. Spartiotis, I. Hietanen, M. Matikkala, S. Eränen and T. Virolainen, *Beam test results of a 60 cm long silicon microstrip detector*, NIM A 364, 1995.

III K. Spartiotis, R. Orava, T. Schulman, J. Pyyhtiä, T. Cao, M. Sarakinos, I. Suni, J. Salonen, L. Grönberg, P. Majander, Z. Karim, D. Allison, B. Sanghera, M. Myers and A. Epenetos, *A direct X-ray digital radiology system for use in mammography, dental imaging, fluoroscopy and conventional X-ray examinations*, Computer Assisted Radiology and Surgery, 1997.

IV K. Spartiotis, R. Orava, T. Schulman, J. Pyyhtiä, M. Sarakinos, B. Sanghera, A. Epenetos, I. Suni, J. Salonen, L. Grönberg, P. Majander, D. Allison and M. Myers, *Novel direct digital modular X-ray device and system*, SPIE Vol. 3336, 1998

V K. Spartiotis, J. Pyyhtiä, T. Schulman, K. Puhakka and K. Muukkonen, *A directly converting high-resolution intra-oral X-ray imaging sensor*, NIM A 501, 2003.

VI K. Spartiotis, T. Schulman and J. Pyyhtiä, *Improvement of the radiation hardness of a directly converting high resolution intra oral X-ray imaging sensor*, NIM A 513, 2003.

VII K. Spartiotis, J. Havunlinna, A. Leppänen, K. Puhakka, T. Pantsar, J. Pyyhtiä and T. Schulman, *A CdTe real time X-ray imaging sensor and system*, NIM A 527, 2004.

VIII K. Spartiotis, A. Leppänen, T. Pantsar, J. Pyyhtiä, P. Laukka, K. Muukkonen, O. Männistö, J. Kinnari and T. Schulman, *A photon counting CdTe gamma- and X-ray camera*, NIM A 550, 2005.

Contribution of the author to the publications

Publications I and II are results of the Si strip detector development of the detector laboratory of the Finnish research institute for high energy physics (SEFT). The author was responsible for the testing of the static parameters of the strip detectors. The author designed and realised automated LabView based I-V, C-V and resistance measurement methods and systems and tested numerous strip detectors. The results presented in figures 4 to 8 of Publication I were acquired by the author. Section 2 of Publication II was written by the author.

Publications III and IV are conference presentations on results of the early stage of the pixel detector development collaboration between the detector laboratory of SEFT and Oy Simage Ltd. The author participated in the overall system design and in the design of the pixel ASIC and the Si and CdZnTe detectors. The author contributed to the development of the thin film pixelisation process of the CdZnTe detectors by monitoring the interpixel resistances. The idea of mounting the pixel detector modules onto ball grid array boards was suggested by the author. The tiling method for large area imaging was invented by the author.

Publication V presents the application of the developed pixel detector technology to an intra oral X-ray imaging sensor. The author contributed to the development of the successful calibration method of the sensor by introducing the 5^{th} order polynomial first stage fit and by suggesting the cooling of the detector during calibration data acquisition. The author wrote a LabView routine which calculated the calibration coefficients for the image reconstruction. The author designed and realised the sensor encapsulation. The author measured and calculated the sensor performance in terms of SNR, MTF and DQE. The author wrote the article.

Publication VI is a description on the problem and solution of the radiation hardness of the intra oral sensor. The author measured the response of the sensor and its components after various radiation doses. The author contributed significantly to the interpretation of the results and to the design change which led to a rad hard intra oral sensor. The author wrote the article.

Publication VII describes the latest version of the developed CdTe real time imager. The author measured and calculated the sensor performance in terms of SNR, NPS, MTF and DQE. The author wrote the article.

Publication VIII presents a novel photon counting CdTe camera suitable for gamma and X-ray imaging with energy discrimination. The author developed a theoretical model to calculate the effect of signal charge diffusion to the signal formation in pixelated CdTe detectors and performed device simulations to find the photo peak efficiency as a function of the detector pixel size. The author contributed significantly to the calibration procedure of the CdTe gamma/X-ray camera and tested and analysed the camera performance in terms of sensitivity, SNR, spatial resolution and photo peak efficiency. The author wrote the article except sections 2.2 and 2.3.

1. Introduction

Since the invention of applying planar technology to semiconductor radiation detector manufacturing [1,2] numerous detector designs have been invented and developed for a wide range of applications both in particle and photon detection. The possibility to process microstructured silicon diode detectors was first utilized in vertex detection in high energy physics experiments [3,4]. Vertex detectors consisting of single sided and later double sided silicon strip detectors arranged in a cylindrical shape around the beam collision point provided position information of the passing ionizing particles with a resolution better than 10 μm [5,6]. The success of silicon detectors in position sensitive particle detection in accelerator experiments soon lead to ideas of applications in other fields of research, medicine and industry. Strip detectors as such were applied to autoradiography [7,8] and tested for X-ray imaging [9,10]. Silicon drift chambers and depleted MOSFET detectors were developed for energy sensitive detection in X-ray spectroscopy [11,12] and a fully depleted CCD X-ray imaging detector has been applied in astrophysics [13]. Pixel detectors which give the advantage over strip detectors of unambiguous position information and higher signal to noise ratio were proposed and have been developed for both particle tracking and X-ray imaging [14,15].

Since digital X-ray imaging offers several advantages over conventional analog film based imaging an immense effort has been invested in research and development of digital X-ray imagers both in the fields of medicine and industry. Commercial state of the art large area systems generally rely on flat panel technology and apply either indirect conversion of X-ray energy with a scintillator [16,17] or direct conversion with amorphous Selenium [18]. Small field detectors which may be combined for scanning configurations are mainly based on optically coupled CCDs [19] but directly converting systems with crystalline semiconductors, CMOS and bump bonding technology have also been developed [20,21]. Directly converting systems yield higher spatial resolution compared to indirect systems [22]. Crystalline semiconductors combined with bump bonding and CMOS electronics allow smaller pixel sizes than flat panel technology but large continuous image areas are impossible with current CMOS technology.

Higher X-ray energies and gamma imaging require a high Z conversion material. Studies on GaAs [23] and HgI_2 [24] have been presented but the most promising high Z materials seem to be CdTe and CdZnTe which have been proposed to be used for example in medical gamma imaging instead of scintillators in order to improve both the spatial and energy resolution of gamma cameras

[25]. High absorption efficiency offers advantages also in real time and scanning imaging or generally in any application where the image acquisition speed or radiation dose is critical.

This work starts with a brief review on Si strip detectors, focuses then on charge integrating Si and CdTe/CdZnTe pixel detectors for digital X-ray imaging and introduces also a novel photon counting CdTe gamma imager. The pixel detector technology presented in this work is based on crystalline semiconductors, bump bonding and CMOS technology and was created mainly at Oy Simage Ltd. and Oy Ajat Ltd., Finland. It evolved from the development of semiconductor detectors at the Research Institute for High Energy Physics (SEFT) [26] which later merged with other physics research units to form the Helsinki Institute of Physics (HIP).

2. Silicon strip detectors

Excellent descriptions on the design and operation of strip detectors are given in [27] and [125] and hence only a brief review of the different types of silicon strip detectors is presented here.

The first silicon strip detectors manufactured with planar technology were simple single sided pin type diode detectors processed on high resistivity n type silicon wafers. The boron implanted hole signal collecting p^+ strips with a typical pitch of 50 μm were directly connected with wire bonds to integrated signal readout circuitry. Later capacitively coupled strip detectors were developed [4] to eliminate the offset variation between strips due to the non-uniform detector leakage current. To improve the position resolution of strip detectors beyond the strip pitch the pulse hight distribution measured from neighbouring strips is used [27, Publication II]. By utilizing interpolation between pulse hights, resolutions better than 5 μm have been achieved [52].

Single sided strip detectors arranged in a cylindrical shape around the beam provide only rφ position information of traversing particles. To measure the z coordinate double sided strip detectors with electron collecting phosphor implanted n^+ strips processed perpendicular to the p^+ strips on the opposite side of the silicon wafer have been developed [Publication I]. While electrical separation of the strips on the junction or p^+ side is naturally achieved under reverse bias, special design is necessary on the ohmic or n^+ side to isolate neighbouring strips from each other. Two approaches have been succesfully used, one implenting floating p^+ regions between and around the n^+ strips [28,29] and the other using negatively biased field plates to repel electrons accumulated at the Si-SiO_2 interface between the n^+ contacts [Publication I]. A special problem occurs when double sided strip detectors are chained to form modules of greater length and detection area. To enable signal readout from the same edge of the detector chip for both sides an additional metal layer with lines perpendicular to the n^+ strips is needed on the ohmic side [Publication I]. A double sided strip detector provides space point information of passing particles. However, if two particles hit the detector within the signal collecting time it is impossible to distinguish the positions of the true hits from the so called ghost hits in the opposite corners of the rectangle defined by the hit positions (see figure 2.1). This ambiguity limits the use of double sided strip detectors to low intensity applications.

Manufacturing double sided strip detectors with high yield especially with the additional metal layer on the ohmic side is difficult and expensive. To overcome manufacturing problems without loosing the rφz measurement ability a design named the single sided stereo detector (SSSD) has been proposed and succesfully realised [30]. Every second p^+ strip of the SSSD is interrupted at an

interval of 1 – 3 mm. The short strips are connected to form inclined stereo strips as shown in figure 2.2. The signal of the stereo strips provides z coordinate information and can also be used in the interpolation of the φ coordinate. The resolution of the z coordinate of the SSSD is not as good as that of the double sided strip detector but the ambiguous ghost hit region of the SSSD is smaller because one inclined strip does not stretch across the whole horizontal dimension of the detector chip.

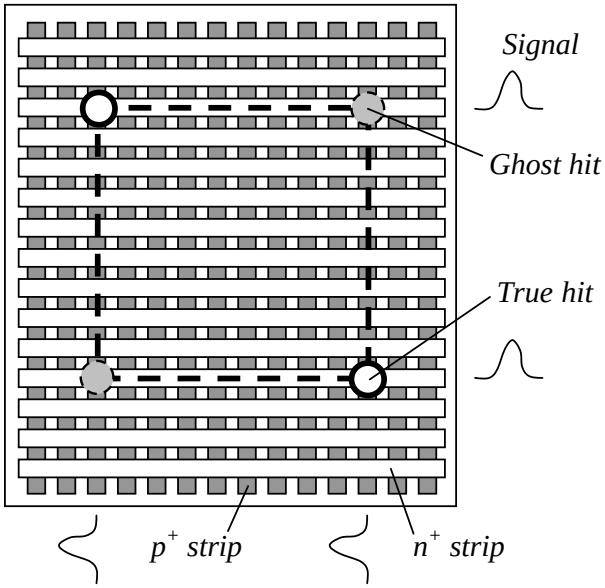


Figure 2.1. Schematic of a double sided strip detector. Two simultaneous hits create signals which could also be induced by hits at the locations of the ghost hits.

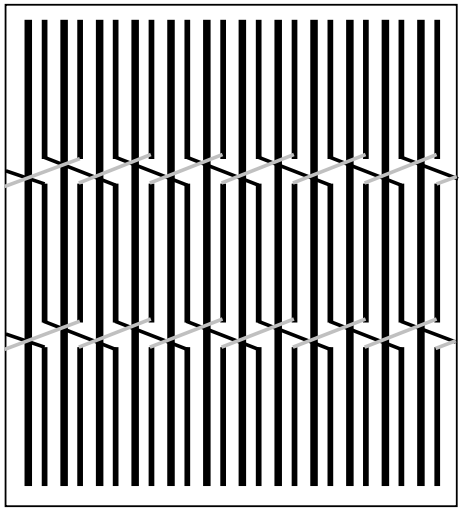


Figure 2.2. Schematic of a single sided stereo strip detector.

To achieve even shorter charge collection times with solid state detectors and to improve charge collection efficiency a 3D electrode design has been proposed [31]. This design is expected to improve the radiation hardness of silicon strip detectors and has therefore recently gained interest [32] as an option to be used in hadron collider experiments. Since the 3D electrode structure demands less bias voltage for full depletion of the detector crystal, signal charge collection becomes possible even from the chip edge region and dead space is thus minimised (figure 2.3).

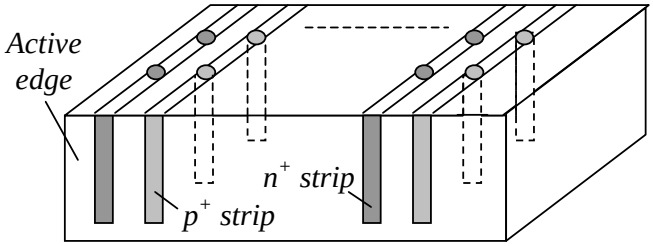


Figure 2.3. Schematic of a 3D electrode strip detector. Holes are etched to extend the p^+ and n^+ strips deep into the crystal bulk for faster and more efficient charge collection.

3. Digital X- and gamma ray imaging

The development of digital detectors for X-ray imaging in general is motivated by the many advantages of digital imaging over analog screen film imaging: digital images are immediately available at the computer display, images can be stored electronically without space consuming hard copies, digital image processing can be used for image enhancement, in medicine doctors may benefit from computer assisted diagnosis and in industry automatic pattern recognition systems may be utilized to spot faults in devices under inspection, fast image transfer through computer networks link remote clinics and central hospitals or inspection and manufacturing units, real time imaging becomes possible, and more contrast information can be collected in one image due to the wider dynamic range of digital detectors than that of film (see section 6.1).

In gamma ray imaging semiconductor detectors are being developed to improve both the position and energy resolution of conventional scintillator-photo multiplier systems.

Different technological approaches have been used to solve the main problems of digital radiation imaging. These problems are related to the position and contrast resolution, conversion efficiency and signal to noise ratio (SNR) of the image receiver and to the large image area required in many applications.

3.1 Direct and indirect conversion of X- and gamma ray energy

Direct detectors convert the radiation energy directly to electrical charge while indirect detectors convert the X- or gamma rays first to visible photons which then in a second stage are converted to charge. The debate on the pros and cons of these competing approaches is both on the imaging performance and on the technological manufacturing problems of the detectors.

Let us first consider an X-ray imaging system operated in the charge integration mode under the effect of a monoenergetic X-ray beam. If S_0 is the image signal as the number of X-rays entering the imaging device then the SNR of the Poisson distributed X-ray field at the device input is

$$SNR_{in} = \frac{S_0}{\sqrt{S_0}} = \sqrt{S_0} \qquad (3.1)$$

If η is the X-ray absorption efficiency of the detecting material and g_1 the conversion gain the signal after conversion is

$$S_1 = \eta g_1 S_0 \tag{3.2}$$

The statistical noise after conversion is the quadratic sum of the noise in the received X-ray field multiplied by the gain and the standard deviation of the converted signal multiplied by the Fano factor F [33] or

$$N_1 = \sqrt{\eta g_1^2 S_0 + F_1 \eta g_1 S_0} = g_1 \sqrt{\eta (1 + \frac{F_1}{g_1}) S_0} \tag{3.3}$$

The zero frequency detective quantum efficiency (DQE, see section 6.1 for details) defined as

$$\varepsilon = \frac{SNR_{out}^2}{SNR_{in}^2} \tag{3.4}$$

is then after the first conversion stage

$$\varepsilon_1 = \frac{(S_1/N_1)^2}{S_0} = \frac{\eta}{1 + \frac{F_1}{g_1}} \tag{3.5}$$

Equation 3.5 gives the ideal zero frequency DQE (or DQE(0)) for the direct conversion method. Since for semiconductor detectors the conversion gain is high and the fano factor less than unity

$$\varepsilon \approx \eta \tag{3.6}$$

for directly converting semiconductor detectors. In indirect systems the first stage is followed by a second in which the light quanta are converted to charge. If g_2 determines the light conversion efficiency and gain then

$$S_2 = \eta g_1 g_2 S_0 \tag{3.7}$$

and

$$N_2 = \sqrt{g_2^2 N_1^2 + F_2 S_2} = g_1 g_2 \sqrt{\eta(1 + \frac{F_1}{g_1} + \frac{F_2}{g_1 g_2})S_0} \tag{3.8}$$

The DQE(0) after the second stage is thus

$$\varepsilon_2 = \frac{\eta}{1 + \frac{F_1}{g_1} + \frac{F_2}{g_1 g_2}} \tag{3.9}$$

In general a system with M stages (e.g., the converting scintillator may be followed by coupling fibers or a lens) has a DQE(0) equal to (statistical limit [40])

$$\varepsilon_M = \frac{\eta}{1 + \sum_{i=1}^{M} \frac{F_i}{\prod_{j=1}^{i} g_j}} \tag{3.10}$$

The conversion gain of scintillators used in indirect systems are much smaller than that of a semiconductor detector but still significantly above unity (the Fano factor of scintillators is close to one). This may not be the case for g_2, e.g., signal loss can occur in optical fibres. However, $g_1 g_2$ is usually >> 1 [19,20,34] and thus the DQE of indirect systems is not significantly affected by the intermediate stages but is close to the X-ray absorption efficiency of the scintillator material. The absorption efficiency is thus naturally of utmost important for any imaging system. Figure 3.1a shows the photo electric absorption efficiency of some semiconductors and scintillator materials. One should remember, however, that the efficiency of directly converting semiconductor detectors can be improved by increasing the absorber thickness without degrading the spatial resolution whereas the scintillator layer has to be relatively thin to maintain image sharpness. Figure 3.1b shows the absorption efficiency of the materials of figure 3.1a at typical thicknesses used in actual devices.

A high conversion gain is a benefit when aiming at high single event SNR but may cause saturation problems at strong radiation intensities if the imaging device is operated in the charge integration mode (see chapter 6).

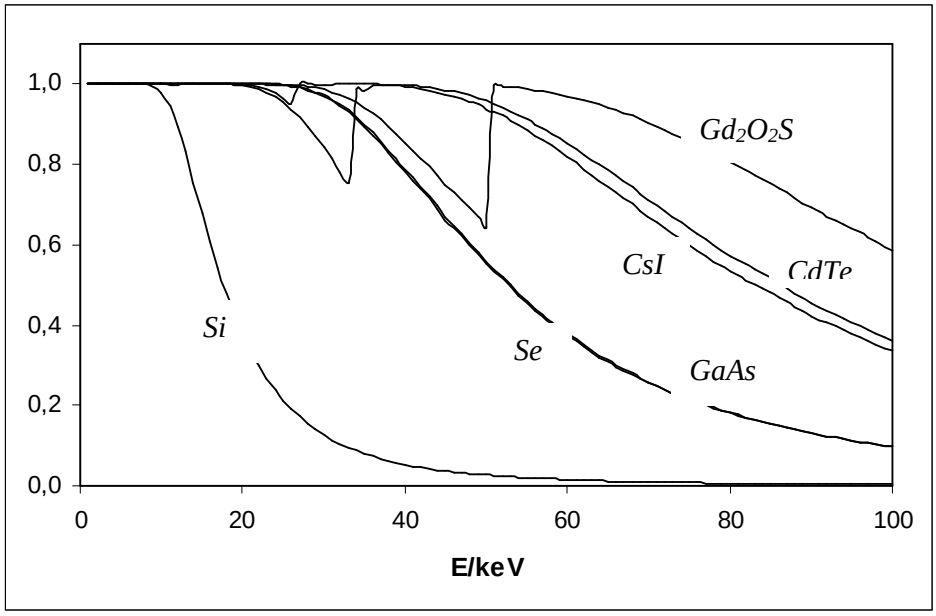


Figure 3.1a. Absorption efficiency of different semiconductor detector and scintillator materials. The thickness of all materials is 0.5 mm.

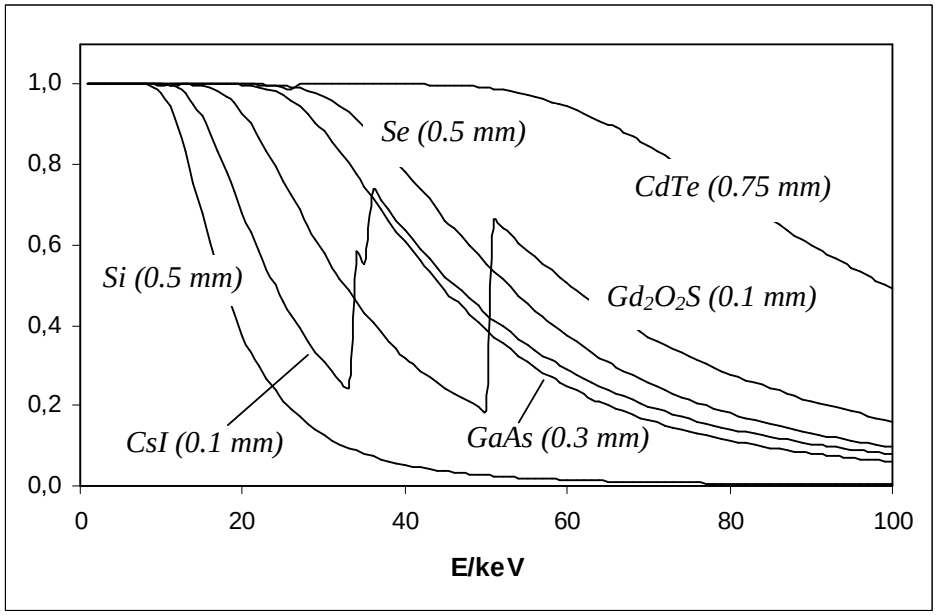


Figure 3.1b. Absorption efficiency of different semiconductor detector and scintillator materials for typical thicknesses used in imaging systems.

The real advantage of the direct conversion method is the minimal lateral signal spread in the converting semiconductor. This results in high spatial resolution and sharp images. When a conventional fluorescent screen is used to convert the X-rays to visible photons a considerable lateral light spread depending on the screen thickness occurs decreasing the spatial resolution. The

thickness of the screen is a compromise between the spatial resolution and the absorption efficiency. Optical fibres [19] or direct columnar deposition of the scintillator material onto the photo detector [35] have been used to reduce the light spread. It is still evident, however, despite some attempts to defend the indirect method [36] by emphasizing the high frequency noise filtration features of the scintillator, that the direct method yields superior image quality [37].

In photon counting applications (e.g., nuclear medicine) indirect systems usually rely on photo multiplier (PM) tubes to count the visible photons emitted by the scintillator. Directly converting semiconductor detectors offer significant performance advantages to such systems [25]. The intrinsic energy resolution of scintillators is worse than that of semiconductor detectors [38] and eliminating the second stage of PM tubes and related statistical loss in the SNR further improves the situation. Semiconductor technology enables also smaller pixel sizes than scintillator-PM tube combinations and offers thus improved spatial resolution along with overall device compactness.

3.2 Photon counting and charge integrating imaging modes

In a photon counting system the image signal is formed by the number of X- or gamma rays detected by the image receiver whereas in a charge integrating (current mode) system the total amount of charge created by the radiation during the imaging time is measured and defines the signal.

Photon counting allows energy distinction in the detected X-ray field which is necessary in certain applications [25,39]. Photon counting requires, however, much more complicated signal readout circuitry and, therefore, in X-ray projection radiography where radiation energy information is not important the charge integration mode is generally preferred although the theoretical contrast resolution and SNR are somewhat better for a photon counting device [41-43].

Let us first consider the contrast. The signal induced by a polyenergetic beam in a charge integrating semiconductor detector is formed as

$$S = \int_0^{E_{\max}} \frac{E}{E_{e-h}} \eta(E) N(E) dE \qquad (3.11)$$

whereas in a photon counting detector all absorbed X-rays are counted as one and the signal can be written as

$$S = \int_0^{E_{max}} \eta(E) N(E) dE \qquad (3.12)$$

In equations 3.11 and 3.12 E is the X-ray energy, η(E) the energy dependent X-ray absorption efficiency of the detector, N(E) the energy distribution of the X-ray beam, E_{max} the maximum energy of the X-rays and $E_{e\text{-}h}$ the energy required to produce one charge carrier pair (electron – hole) in the detector crystal.

To compare the contrast resolution of the two methods let us consider the imaging of an object of thickness d_1. The measured contrast of the object is defined as

$$C = \frac{S_0 - S}{S_0 + S} \qquad (3.13)$$

where S_0 is the signal detected around the object and S is the signal detected under the object (see figure 3.2). Let μ_1 be the X-ray attenuation coefficient of the object and μ_2 and d_2 the attenuation coefficient and thickness of the detector, respectively. Then, according to equations 3.11 and 3.12, if $I_0(E)$ is the intensity distribution of the X-ray field before the object, the signals S_0 and S for the charge integration method can be written as

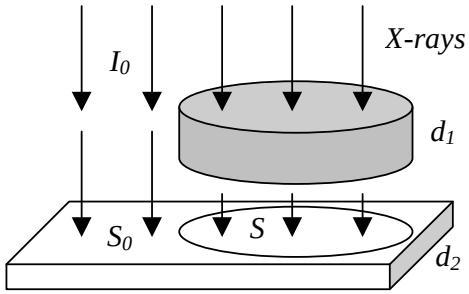


Figure 3.2. Imaging of an object with thickness d_1.

$$S_0 = \int_0^{E_{max}} \frac{E}{E_{e-h}} (1 - e^{-\mu_2 d_2}) I_0 dE$$
$$S = \int_0^{E_{max}} \frac{E}{E_{e-h}} (1 - e^{-\mu_2 d_2}) I_0 e^{-\mu_1 d_1} dE \qquad (3.14)$$

and for the photon counting method as

$$S_0 = \int_0^{E_{max}} (1 - e^{-\mu_2 d_2}) I_0 dE$$
$$S = \int_0^{E_{max}} (1 - e^{-\mu_2 d_2}) I_0 e^{-\mu_1 d_1} dE \qquad (3.15)$$

The measured contrasts for the two methods (int for integration and ph for photon counting) as defined by equation 3.13 are

$$C_{int} = \frac{\int_0^{E_{max}} EI_0(1-e^{-\mu_1 d_1})(1-e^{-\mu_2 d_2})dE}{\int_0^{E_{max}} EI_0(1+e^{-\mu_1 d_1})(1-e^{-\mu_2 d_2})dE}$$
$$C_{ph} = \frac{\int_0^{E_{max}} I_0(1-e^{-\mu_1 d_1})(1-e^{-\mu_2 d_2})dE}{\int_0^{E_{max}} I_0(1+e^{-\mu_1 d_1})(1-e^{-\mu_2 d_2})dE} \qquad (3.16)$$

Plotting C_{int} and C_{ph} for various X-ray fields, objects and detectors shows that $C_{int} < C_{ph}$ as is demonstrated in figure 3.3 for a 0.5 mm thick silicon detector and a 60 kV X-ray beam filtered with 1 mm aluminium.

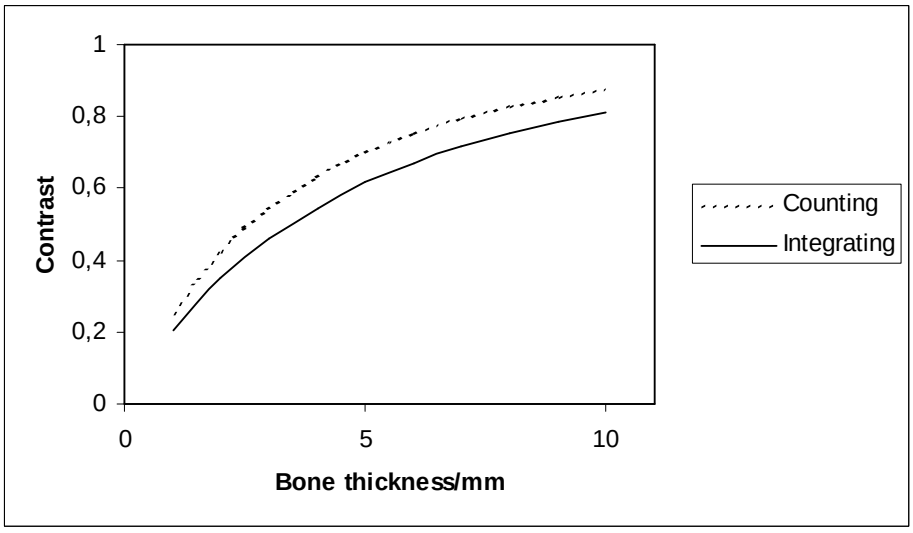


Figure 3.3. Simulated contrast as a function of human bone thickness for the photon counting and the charge integration imaging methods.

The reason to the reduced contrast of the integration method is the weight given to the higher energy X-rays which carry less contrast information than the lower energy X-rays.

Secondly we compare the signal to noise ratios. The noise in a photon counting detector is ideally the square root of the absorbed number of X-rays, i.e., the quantum noise in the absorbed Poisson distributed X-ray field. Then the SNR is

$$SNR_{ph} = \frac{\int_0^{E_{\max}} \eta(E)N(E)dE}{\sqrt{\int_0^{E_{\max}} \eta(E)N(E)dE}} = \sqrt{\int_0^{E_{\max}} \eta(E)N(E)dE} \tag{3.17}$$

The noise in a charge integrating detector is the deviation in the total induced energy. The SNR is thus (the noise originating from the conversion process is insignificant as was seen in the previous section and is neglected here)

$$SNR_{int} = \frac{\int_0^{E_{\max}} \frac{E}{E_{e-h}} \eta(E)N(E)dE}{\sqrt{\int_0^{E_{\max}} (\frac{E}{E_{e-h}})^2 \eta(E)N(E)dE}} = \frac{\int_0^{E_{\max}} E\eta(E)N(E)dE}{\sqrt{\int_0^{E_{\max}} E^2\eta(E)N(E)dE}} \tag{3.18}$$

The DQE(0) for the two cases is then (as defined in equation 3.4)

$$\varepsilon_{ph} = \frac{\int_0^{E_{\max}} \eta(E)N(E)dE}{\int_0^{E_{\max}} N(E)dE}$$

$$\varepsilon_{int} = \frac{\left(\int_0^{E_{\max}} E\eta(E)N(E)dE\right)^2}{\int_0^{E_{\max}} E^2\eta(E)N(E)dE \int_0^{E_{\max}} N(E)dE} \tag{3.19}$$

Figure 3.4 shows two examples of simulated DQE(0). The DQE of photon counting detectors is slightly better than that of charge integrating ones. However, if energy discrimination is applied in a photon counting detector and if the detector pixel pitch is small, a significant part of the radiation hits may be lost due to charge sharing between pixels reducing the SNR of photon counting devices (see section 6.4). Charge sharing and incomplete signal charge collection are not problems in charge integrating detectors which therefore allow the use of very small pixel sizes.

Charge integrating detectors are not limited by the radiation intensity as long as the signal charge integration capacity is not exceeded. Digital counters up to 15 bits have been implemented at

each pixel on photon counting readout circuits to enable imaging at higher dose rates [44] but processing the signals of individual photons always requires some minimum shaping time which sets an upper limit to the intensity and may be a problem in some applications.

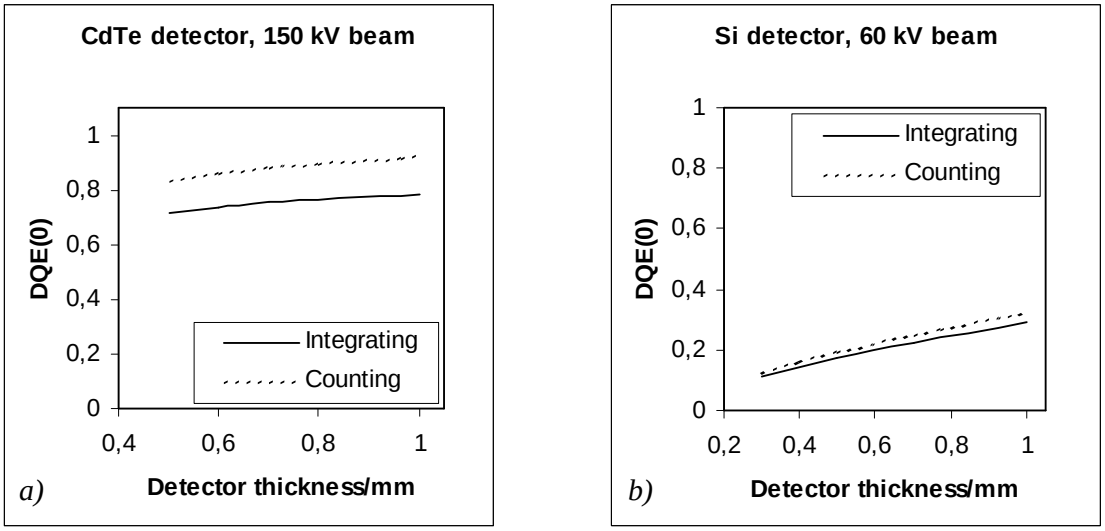


Figure 3.4. Simulated DQE(0) as a function of detector thickness for a) a CdTe detector (150 kV X-ray tube voltage) and b) a silicon detector (60 kV tube voltage). The X-ray beam was filtered with 1 mm aluminum.

3.3 Large area imaging

For any digital X-ray imaging system a considerable challenge is the requirement of a large uniform imaging area without any dead regions. Large area imagers based on amorphous semiconductor and flat panel technology have been developed and are commercially available [16-18]. Crystalline semiconductor detectors and CMOS technology offer better image quality but do not allow large continuous image areas as is the case also for CCD based systems. Large area lens coupled CCD systems have been developed [50] but such systems suffer from relatively poor spatial resolution.

To achieve larger image coverage with crystalline semiconductors and CCDs scanning solutions have been developed [19,45,46]. A scanning X-ray imager can fairly easily be constructed by arranging small field pixel detectors or fiber optically coupled CCDs side by side in a slot like configuration. Scanning as an X-ray imaging method brings the advantage of good scatter rejection which is important for example in mammography. To reduce the imaging time the time delay integration (TDI) method has been applied [20]. The imaging time of a scanning device is always, however, inferior to that of a single frame imager.

Large area imaging with area or step scanning has also been proposed in which full image coverage is achieved by moving a mosaic of detectors in a few steps under a pulsed X-ray source [47]. One part of this work was a contribution to the development and testing of a step scanning system prototype [48, Publications III and IV]. In this system the individual detector tiles are arranged on the master plane as shown in figure 3.5. The active detector areas cover one third of the complete image plane. Mounting the detector columns shifted up and down allows the image to be taken with three snapshots by moving the master board in only one direction. A collimator can be used to protect tissue regions above the dead space of the detectors and the X-ray source can be turned off during masterboard movement. With a powerful and accurate translation stage the imaging time can be kept at 1 s. However, even if possible to realise, the system is cumbersome and problems related to alignment of the detector tiles and to the dose difference between the succesive X-ray exposures makes it less attractive for commercial use.

Other tiling techniques aiming at larger imaging areas without involving master board movement are explained in sections 4.5 and 5.3. Experience indicates that small field imagers (few tens of cm^2) for commercial applications are possible utilizing tiling methods but truly large area imaging with crystalline semiconductors and CMOS technology is only possible with scanning.

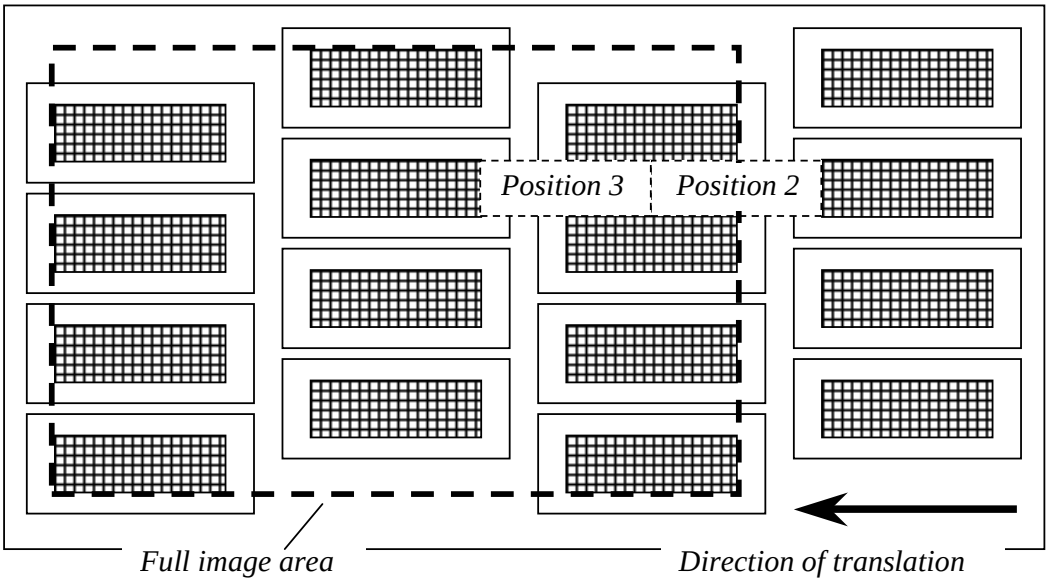


Figure 3.5. Schematic of a tiling configuration for large area imaging. The master board is moved in two steps and one snapshot image is taken at each position. The three acquired images are then combined off line to form the full field image [Publication III].

4. Charge integrating silicon pixel detectors

This work contributed to the development of charge integrating high resolution silicon pixel detectors for digital X-ray imaging. The development has resulted in a generic and versatile design of a silicon pixel detector which can, with slight modifications, be used in several applications. As an X-ray absorber silicon is suitable for low X-ray energies used, e.g., in mammography and for moderate energies up to 60 keV if sensitivity is not of crucial importance.

4.1 Detector design

The silicon pixel detector design used in this work is a simple monolithic array of dc coupled pin diodes surrounded by a guard ring. The pixel size is 35 μm but any other pixel size would naturally also be possible. The ultimate limit to the pixel size of a detector operating in the charge integrating mode is determined by the diffusion of the signal charge carriers. The lateral spread of the charge carriers depends on the detector bias voltage and can be estimated by the solution of the diffusion equation [53]. The standard deviation of the gaussian distributed signal charge cloud arriving at the detector electrodes is typically around 10 μm for Si pin detectors. Thus the pixel size is in practice limited by manufacturing problems rather than by the intrinsic properties of the detector crystal (see next section). A pixel size of 35 μm is close to the manufacturable limit and yields a theoretical spatial resolution of 14.3 lp/mm which is adequate for most if not all medical and industrial applications. Figure 4.1 shows the layout and cross section of one corner of a Si pixel detector. The p^+ implantations are covered with an aluminum contact pad. The detector chip is passivated with SiO_2. The guard ring design was chosen according to the requirement to minimise dead space at the detector edge. Therefore, a single guard ring was implented instead of an optimised multi guard ring structure [50].

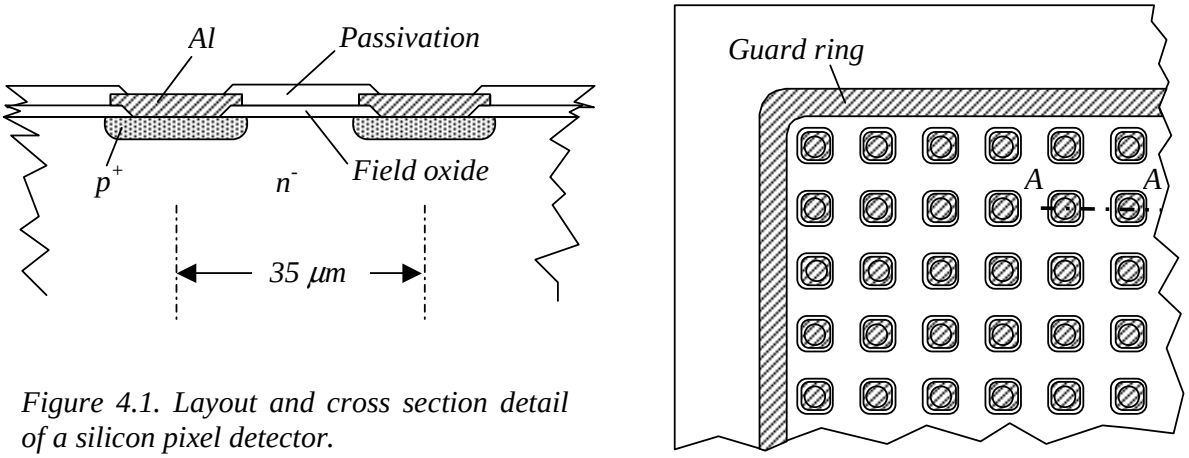


Figure 4.1. Layout and cross section detail of a silicon pixel detector.

To avoid edge leakage current at full depletion the distance from the guard ring to the chip edge should be at least equal to the thickness of the detector. In certain applications, however, it may be necessary to dice even closer to the guard ring for minimum dead space. In such a case it is beneficial to use lower reverse bias voltage and to deplete the detector only partially. Experience has shown that signal charge created in the undepleted region is collected with remarkable efficiency [51]. This is especially true for a charge integrating detector with a long signal integration time of several hundreds of ms.

4.2 Bump bonding and sensor module structure

For signal readout the Si pixel detectors are flip chip or bump bonded to charge integrating CMOS amplifiers. The CMOS circuit chips are then mounted onto printed circuit boards. The resulting sensor module structure is shown in figure 4.2. The size of such a module is limited by the detector and CMOS processing technology. Conventional CMOS technology allows a maximum circuit size of a few cm^2. Si pixel detectors can in principle be as large as one high resistivity silicon wafer (diameter 10 – 15 cm). It is possible to flip chip connect many CMOS circuits to one pixel detector to obtain a larger continuous imaging area (see section 4.5).

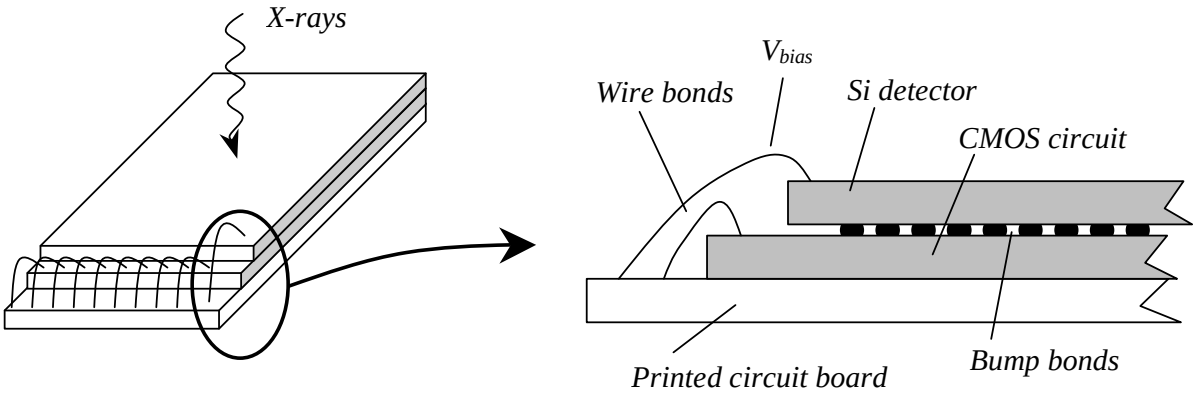


Figure 4.2. The structure of the Si pixel X-ray imaging sensor

The material of the micro bumps can be either In or Pb/Sn (solder). Indium bumps are created on the pixel contacts of both the CMOS circuit and the Si detector by evaporation and lift off. The flip chip connection with In bumps is performed by mechanically pressing the two aligned chips together. Pb/Sn bumps are grown by electrolytic means on the CMOS pixels only. Prior to the solder bump growth an under bump metal (UBM) layer is applied to the pixel contacts to ensure adhesion and wetting and to prevent diffusion of the solder into the silicon bulk. For solder bumps

the UBM layer (e.g., TiW/Ni/Au) is necessary also on the pixel contacts of the Si detector. Figure 4.3 shows a top view and cross section of two detector pixels with the UBM layer.

Bump bonding of 35 μm pixels demands high alignment accuracy of the flip chip bonder. Since the pixel matrix may contain hundreds of thousands of pixels surface cleanness is of utmost importance. A dust particle or a lithography defect on a single pixel contact (see figure 4.4) may cause the failure of the flip chip connection of the whole sensor.

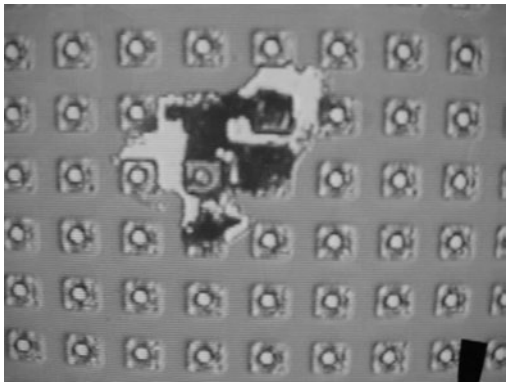


Figure 4.4. Lithography defect on the surface of a Si pixel detector.

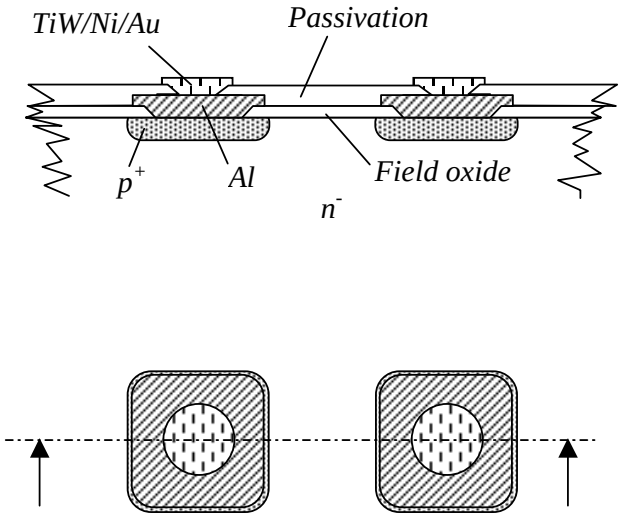


Figure 4.3. Si detector pixels with UBM.

To ensure adequate mechanical strength of the bump bonded detector module under fill is applied between the CMOS and the detector chips. Due to the high bump density very low viscosity is required of the under fill material.

4.3 Front end CMOS circuitry and signal readout

The X-ray induced positive signal charge in the detector crystal is transported by the applied electric field through the bump connection to the CMOS amplifier input. The CMOS pixel cell consists of three MOS field effect transistors as shown in figure 4.5.

Prior to charge signal integration the gate voltage of T2 is reset to V_{reset} which is typically +1.5 V. The reset switch T1 is then closed, V_{reset} is raised to +5 V and signal integration starts. (For negative signal acquisition the reset voltage is +5 V and is kept constant.) When the switch T3 is opened a current signal proportional to the integrated charge flows through T2. Following readout, T2 is reset again and is immediately active for additional charge integration. Multiple signal frames may thus be collected during the same X-ray exposure allowing imaging with large dynamic range. The diodes D1 and D2 protect the pixel cell against overload and static electricity shocks.

Figure 4.6 shows the readout configuration of the pixel matrix. The switches T3 connects the pixel rows sequentially to the column buses which are multiplexed to one common AD converter. The reset follows the readout and is performed simultaneously for all the pixels of one row.

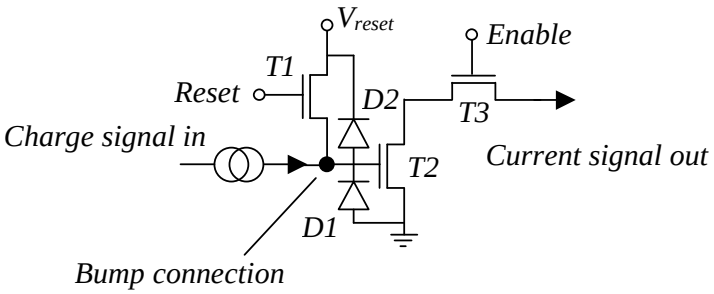


Figure 4.5. Circuit diagram of the CMOS pixel cell.

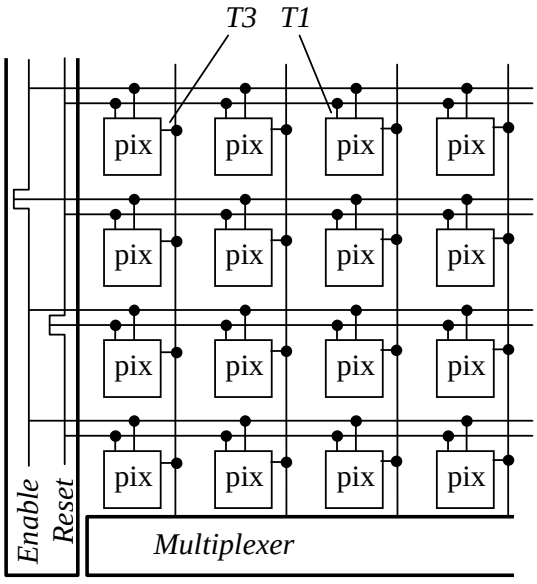


Figure 4.6. Signal readout and reset configuration of the pixel matrix.

In operation the readout and reset cycle runs continuously and pixel signals are stored in an off chip buffer. The start of data frame pixel is marked either externally by synchronizing the X-ray exposure and the signal readout or internally by monitoring the X-ray induced rise in the total detector reverse current. To collect the complete integrated charge signal at least two frames need to be acquired. This is illustrated in figure 4.7. If the X-ray exposure is longer than the readout time of one frame then a third (or more) frame is added.

To cover larger image areas sensor modules or tiles can be connected in parallel if high readout speed is required (e.g., scanning applications) or alternatively serially chained to one output channel.

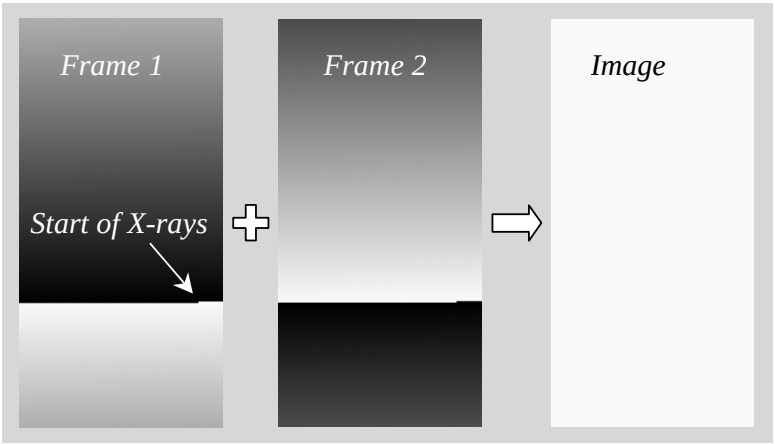


Figure 4.7. Illustration of signal readout for a sensor module with 256 x 128 pixels. The arrow points at the start of frame location. The readout direction is from right to left and down to up.

4.4 Calibration and image acquisition

Due to non-linearity in the response of the front end MOSFETs, to CMOS process mismatch problems and to non-uniformity in the resistivity of the detector crystal calibration of the imaging sensor is necessary.

At a first stage, the response of each CMOS pixel cell is measured as a function of the input gate voltage. This could be done before the bump bonding of the readout circuit to the detector chip but since the connected detector affects the total input capacitance the calibration data has to be collected from a complete sensor module. To minimise the effect of the detector leakage current the module is first cooled down close to 0 °C. The pixel responses are then measured by applying different reset voltage values to the input gates and by recording the corresponding output currents as ADC counts. An example of a measured gate voltage vs. ADC plot is shown in figure 4.8. The response functions are obtained by polynomial least square fits to the measured data as

$$V_{gate} = f_1(ADC) \tag{4.1}$$

The function f_1 gives the voltage at the input gate for a measured ADC value for a specific pixel. The order of the polynomials is a compromise between the efficiency of fixed pattern noise removal and image reconstruction speed. Figure 4.8 shows an example of a third order polynomial fit for which f_1 takes the form

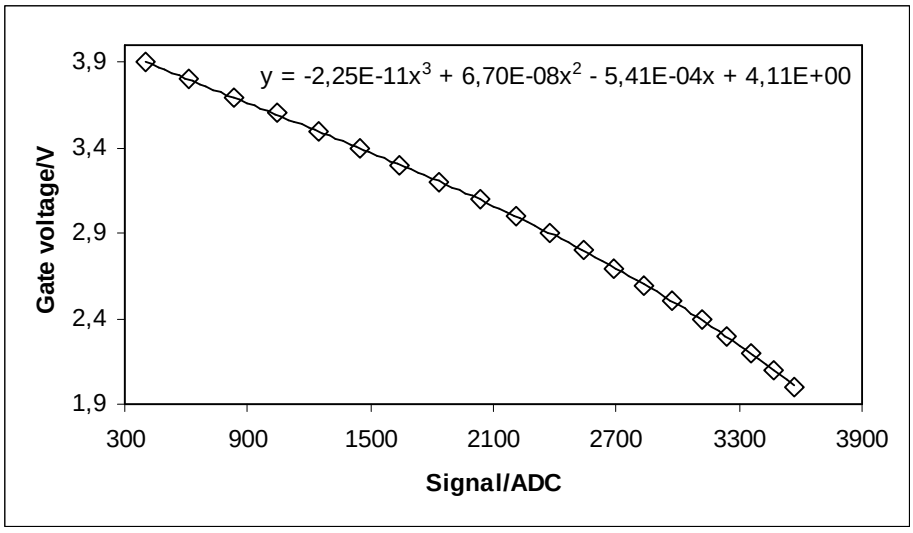


Figure 4.8. Calibration data of one pixel for the determination of the gate voltage as a function of measured output signal.

$$f_1 = a + bADC + cADC^2 + dADC^3 \quad (4.2)$$

The second stage in the calibration yields a function to convert the gate voltage values to X-ray exposure. Because of variation in the resistivity of the silicon crystal the thickness of the depletion layer is not uniform. The absorption efficiency of the detector depends on the depletion layer thickness and thus the amount of induced signal charge is not necessarily the same in different regions of the detector. Calibration data for the second stage is collected from the detector at room temperature at different exposures from zero dose (dark image) to the near saturation dose. The acquired ADC values for each pixel are first converted to voltage at the input gate according to the function f_1. For one image two signal frames and one dark frame are collected and the image reconstruction is done as illustrated in figure 4.7. The result is an image consisting of the pixel gate voltage values:

$$V_{gate} = f_1(frame_1) + f_1(frame_2) - 2 \cdot f_1(dark\ \ frame) \quad (4.3)$$

Polynomial least square fits are then performed to obtain the relation between the gate voltage and the exposure for each pixel. If the exposure is defined as induced charge in the detector the function

$$Q_{pix} = f_2(V_{gate}) = f_2(f_1(ADC)) \quad (4.4)$$

where Q_{pix} is the integrated charge at the input gate is in theory linear (Q = CV, where C is the input capacitance) but practice has shown that a second order polynomial fit gives better results.

The different exposures needed for the calibration data can be defined either by changing the X-ray tube current or the exposure time or then by using a set of filters between the tube and the detector at constant tube current and exposure time. Since the X-ray tube adjustments are rather coarse more accurate results are obtained by using filters (for example a stack of polished silicon wafers with accurate and uniform thickness). The exposure for a specific filter defined as induced charge in the detector crystal is given by

$$Q = \int N(E) e^{-\mu_{filt}(E) d_{filt}} (1 - e^{-\mu_{det}(E) d_{det}}) \frac{E}{E_{e-h}} q dE \quad (4.5)$$

where N(E) is the X-ray spectrum, E the X-ray energy, $E_{e\text{-}h}$ the energy required to create one charge carrier pair in the detector, q the elementary charge, $\mu_{filt}(E)$ and $\mu_{det}(E)$ the X-ray attenuation coefficients and d_{filt} and d_{det} the thickness of the filter and the detector, respectively. Because of the quantum noise in the X-ray field the average of several acquired calibration images is used in the fit to obtain f_2 as

$$f_2 = g + hV_{gate} + iV_{gate}^2 \tag{4.5}$$

Figure 4.9 shows an example of the determination of f_2 for one pixel.

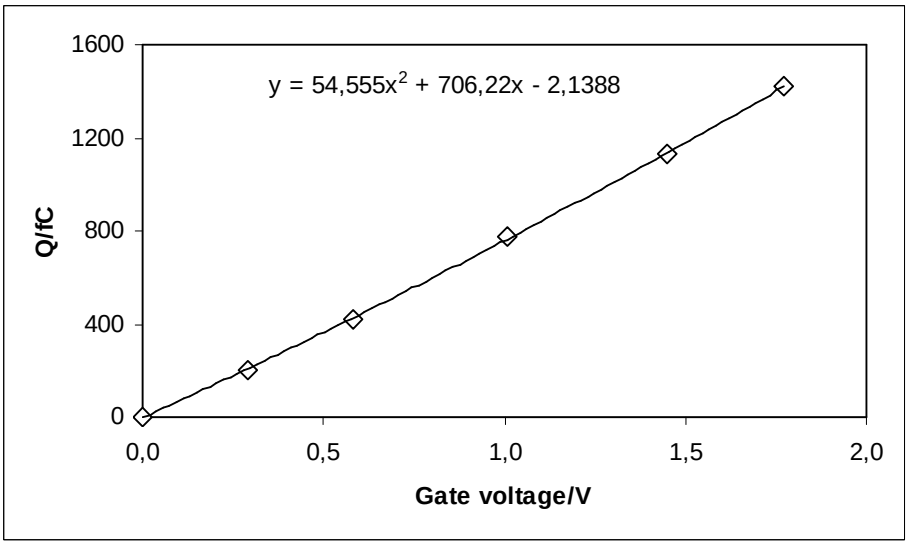


Figure 4.9. Calibration data of one pixel for the determination of the acquired signal charge as a function of the input gate voltage.

The calibration data (i.e., the polynomial coefficients) is finally stored in a file to be used in the image reconstruction. In the general case of N acquired data frames the reconstructured image is given by

$$image = f_2(f_1(frame_1)) + \ldots + f_2(f_1(frame_N)) - N \cdot f_2(f_1(dark\ \ frame)) \tag{4.6}$$

and can be scaled for example to a 16 bit image as

$$image16 = \frac{65536}{Q_{\max}} image \tag{4.7}$$

The fit residual data of the second stage fit can be used to automatically create a mask file to eliminate dead pixels. Figure 4.10a shows the distribution of the residuals of a second stage fit. Residuals not falling within the gaussian distribution indicate pixels which are not responding to radiation. The mask file in which pixels with residuals higher than a predefined threshold are marked as white is shown in figure 4.10b. The image value of a dead pixel is calculated as the average value of the neighbouring pixels.

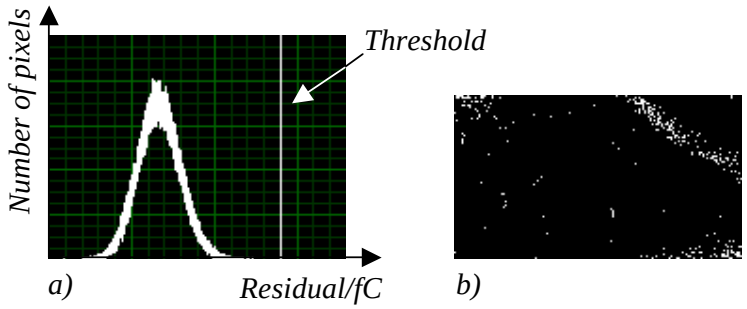


Figure 4.10. a) An example of the distribution of the fit residuals of the second stage fit. b) Mask image used to eliminate dead pixels.

4.5 Application to dental intra oral X-ray imaging

Dental intra oral X-ray imaging applies moderate X-ray energies generated by tube voltages of typically 60 – 70 kV. High spatial resolution is desired and hence X-ray film is used without a converting screen in conventional intra oral X-ray imaging despite the low absorption efficiency of bare film. Digital X-ray imaging is attractive to the dentist because of immediate image display without the need of chemical film development. State of the art digital intra oral X-ray imagers are based on scintillator and CCD technology [54]. The advantages offered by the directly converting silicon pixel detector technology described in the previous section are the large dynamic range (no saturation problems) and the compact sensor structure (thin sensor) possible without compromising the spatial resolution.

As described in [Publication V] the intra oral sensor prototype of this work consists of six CMOS readout circuits bump bonded side by side to one silicon pixel detector. The number of pixels of one CMOS circuit is 272 x 512 = 139,264. The total number of pixels is then 835,584 and the active sensor area is 3.6 x 2.9 = 10.44 cm^2 which corresponds to the standard dental film size 2. The overall pixel size is 35 μm but four rows of larger pixels (35 x 70 μm^2) are implemented in each region between two adjacent readout circuits. These larger pixels are necessary in order to make space for control wires on the CMOS chip and to improve the dicing yield of the CMOS wafers. Dicing is very critical since the dead space allowed at the edge of the CMOS circuits to be

bump bonded side by side onto the Si pixel detector is very small. The bump bonded sensor is glued onto a ceramic board and encapsulated in epoxy and a plastic cover as shown in figures 4.11 and 4.12.

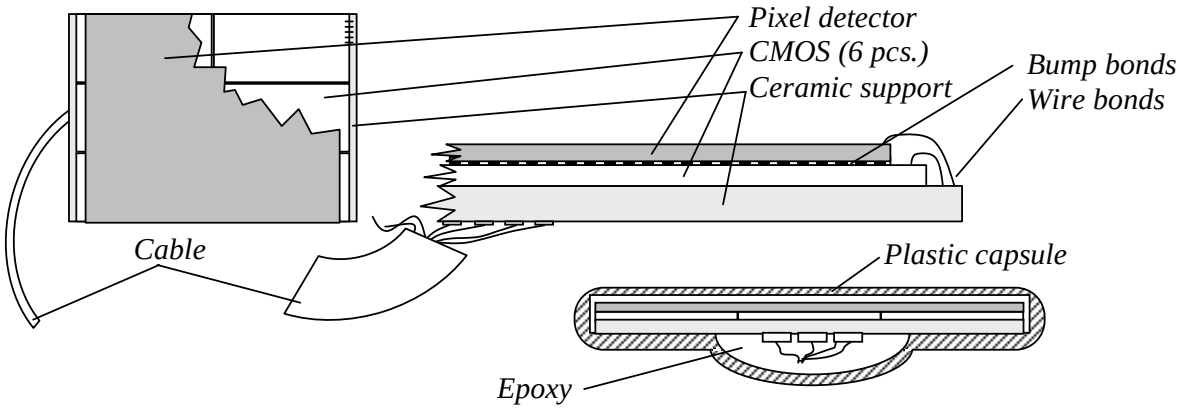
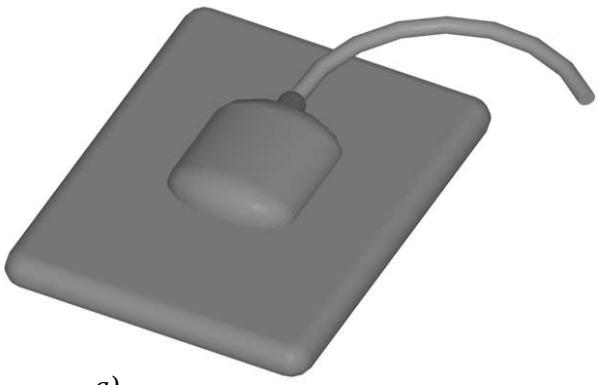
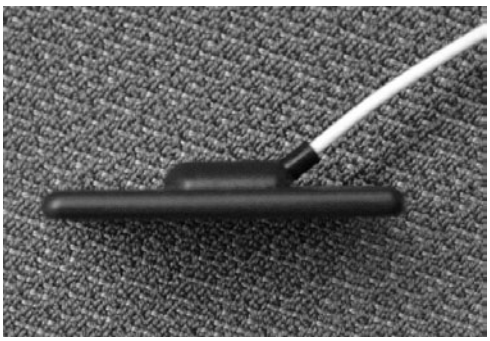


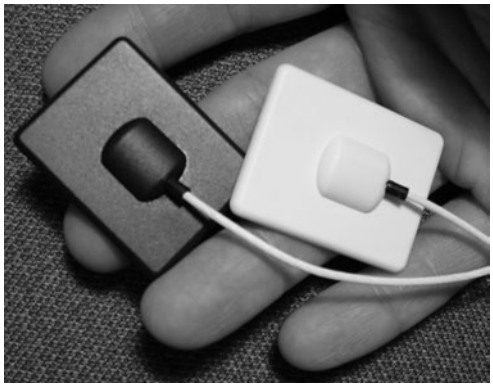
Figure 4.11. Structure of the dental intra oral prototype sensor.



a)



b)



c)

Figure 4.12. a) Autocad drawing of the intra oral sensor capsule. b) and c) Photographs of the encapsulated sensor.

The sensor is connected with a thin cable to a control unit which in turn is connected to the host computer via the Universal Serial Bus (USB) port. The signal readout configuration and data acquisition of the intra oral sensor is described in more detail in [Publication V].

A special calibration problem is caused by the different response of the larger pixels compared to the smaller pixels. While the overall fixed pattern noise is efficiently removed with a third order polynomial fit at the first calibration stage experiments have shown that the complete visible elimination of the lines in the image due to the larger pixels (see figure 4.13) requires a fifth order polynomial function $V_{gate} = f_1(ADC)$.

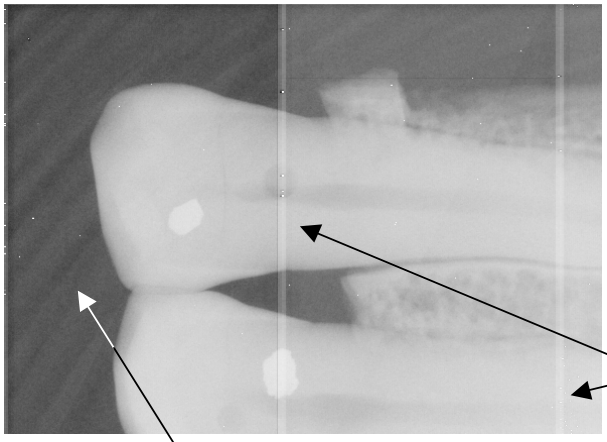


Figure 4.13. Part of an image (negative) of a teeth phantom acquired with the intra oral sensor before calibration. The lines between two CMOS circuits are caused by the different response of the larger pixels compared to the small pixels. The pattern at the left side shows the resistivity variation of the silicon detector wafer.

In the image the large pixels consist of two adjacent image pixels which in reality should have the same gray value. However, in order to hide as completely as possible the large pixels from the image artificial noise is added to the neighbouring image pixels forming the large pixel. The artificial noise is created during the calibration process by using two different sets of image frames when averaging the calibration data for the second stage fit. In this way two different functions f_2 are obtained for one large pixel. These functions are then used to create two neighbouring small pixels with a slightly different grey value to form the large pixel. This is illustrated in figure 4.14 which shows the X-ray image of the head of a mouse surrounded by its tail and a detail of the tail. The calibration has efficiently removed the fixed pattern noise and the large pixels are hardly distinguishable even in the enlarged view of the tail detail.

The performance analysis of the intra oral sensor is presented in section 6.2. The sensor exhibits very high spatial resolution and is quantum limited at typical dental exposure levels. The technology has thus great potential of being the solution for the next generation digital intra oral

sensors. Figure 4.15 illustrates the sensor performance by showing an X-ray image of a teeth phantom.

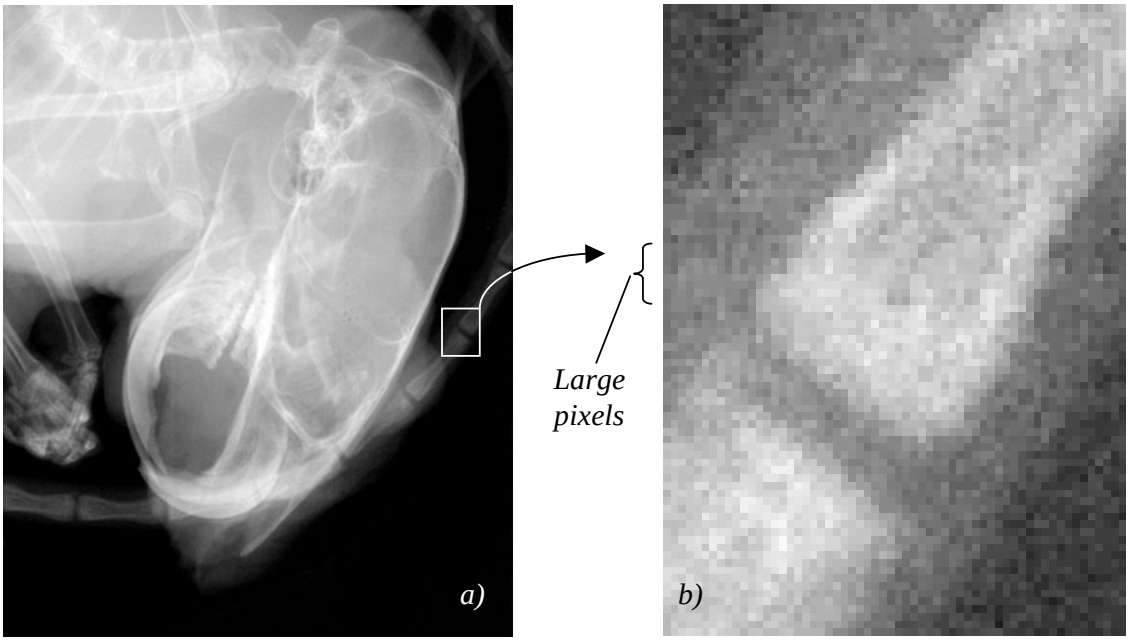


Figure 4.14. a) An X-ray image of the head of a mouse acquired with the intra oral sensor [96]. b) An enlarged view of a detail of the mouse tail. The enlarged view is from a region crossed by the large pixels.

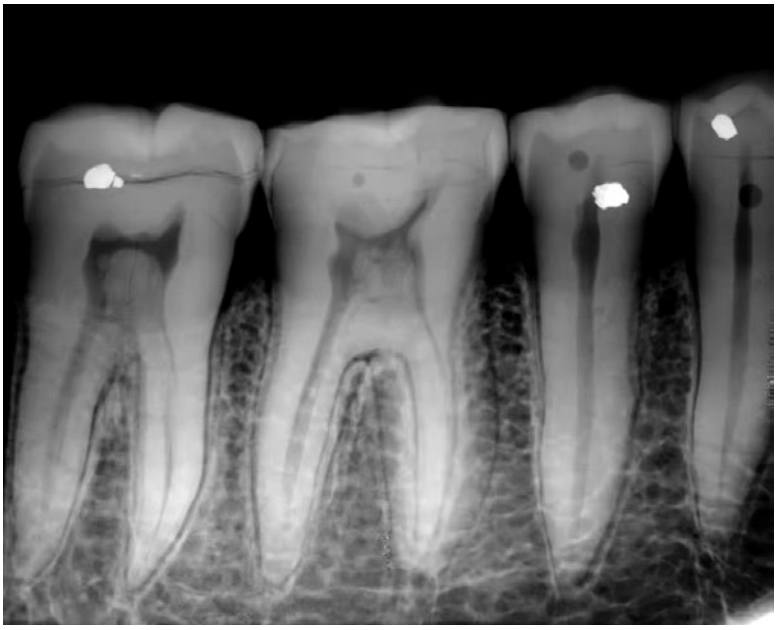


Figure 4.15. X-ray image of a teeth phantom (local transform domain denoising filter applied for image enhancement [94]).

5. CdTe and CdZnTe pixel detectors

The development of CdTe and CdZnTe pixel detectors for imaging applications is motivated by the high X-ray absorption efficiency of these compound semiconductors. The possibility of simultaneously maintaining high spatial resolution and efficiency for a wide X-ray energy spectrum with a single imaging device is attractive. As a detector material CdTe and CdZnTe are not, however, as mature as silicon. This is particulary true for large field pixel detectors when crystal uniformity is of crucial importance [55,63,71].

The world wide development of CdTe/CdZnTe detectors focused first on single channel detectors for X- and gamma ray spectroscopy [56,57] but multi channel devices for gamma cameras in nuclear medicine and other applications have also been introduced both as multi element pixel arrays [58,122] and as single element monolithic arrays [59-61,123]. Since gamma camera detectors are operated in the pulse counting mode and the pixel size is in the mm^2 range the pixelisation process for monolithic devices is less demanding than in X-ray imaging. X-ray imaging requires sub mm spatial resolution and is perfomed in the charge integration mode which puts special demands on the surface resistivity of the CdTe/CdZnTe detectors. Consequently fewer works exist on the development of CdTe/CdZnTe pixel detectors for X-ray imaging [21,48,91,92,Publications III,IV and VII].

5.1 Material properties

The large bandgap energy of CdTe of 1.52 eV allows room temperature detector operation even without rectifying electrodes. Detector grade CdTe crystals are usually grown with the traveling heater method (THM) [55,62,68]. High resistivities up to 10^9 Ωcm are achieved by Cl doping to compensate impurities. The life time (τ) and mobility (μ) of the signal charge carriers (electrons (e) and holes (h)) which determine the signal charge collection efficiency and affect the detector performance have been reported recently as τ_e = 2 - 3 μs, τ_h = 2 μs, μ_e = 1100 cm^2/Vs and μ_h = 100 cm^2/Vs [64,65].

The relatively low hole mobility and life time cause hole trapping and consequent signal charge loss. The amount of signal charge loss in a single X- or gamma event and hence the signal strength depend on the interaction depth of the absorbed photon. In energy sensitive measurements this results in an assymetric broadening of the spectral peaks toward the low energy direction. This effect is more severe for higher gamma energies due to the more uniform interaction depth

distribution of energetic gamma rays. Charge collection efficiency can be improved by increasing the electric field strength in the detector crystal as can be seen from the Hecht equation [66]

$$\frac{q}{eN_0} = \frac{E}{L}(\mu_e\tau_e(1-e^{(L-x)/E\mu_e\tau_e}) + \mu_h\tau_h(1-e^{-x/E\mu_h\tau_h})) \qquad (5.1)$$

which describes the induced charge signal at the anode electrode of a planar radiation detector when x is the photon interaction depth measured from the cathode, L is the detector thickness, E the electric field, e the elementary charge and N_0 the number of signal charge carriers created in one photon interaction. Equation 5.1 gives the ratio of the collected signal charge to the induced signal and is plotted in figure 5.1 as a function of the field strength for three different interaction depths.

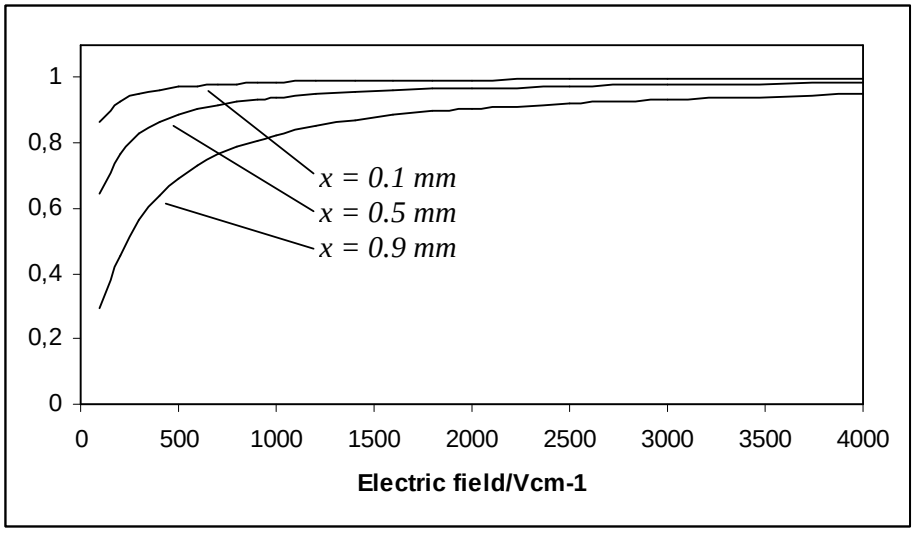


Figure 5.1. The ratio of the collected to the induced signal charge as a function of the electric field in the detector crystal according to the Hecht relation ($\mu_e\tau_e$ =3.3·10^{-3} cm^2/V, $\mu_h\tau_h$ =2.0·10^{-4} cm^2/V and L = 1.0 mm).

It is evident that the charge collection efficiency improves and the signal strength dependency on the interaction depth decreases with increasing field strength. However, if the detector electrodes form ohmic contacts with the CdTe crystal the detector leakage current is directly proportional to the electric field. The leakage current shot noise eventually becomes the dominant noise source and prohibits higher field strengths.

CdZnTe was developed to reach higher resistivities and lower leakage currents than are possible with CdTe. Varying the Zn concentration the band gap can be streched up to 1.64 eV and the resistivity elevated to 10^{11} Ωcm. Despite the drawback of much lower hole life time of CdZnTe

(τ_e = 3 - 7 μs, τ_h = 50 – 300 ns, μ_e = 1350 cm^2/Vs and μ_h = 120 cm^2/Vs) compared to CdTe improved energy resolution has been demonstrated with CdZnTe detectors. A major problem of the high resistivity CdZnTe crystals which are generally grown by the high pressure Bridgeman (HPB) [63,65,71] technique is the crystal non-uniformity [71]. Crystal defects such as grain boundaries reduce the yield especially in imaging applications where large area detectors are required.

More recently CdTe detectors with Schottky type rectifying metal contacts have been introduced [67,70]. Reverse biasing a Schottky type CdTe detector greatly reduces the leakage current and operation at much higher electric fields becomes possible. A Schottky barrier contact on p type CdTe can be formed for example by evaporation of indium [67,69]. Significantly enhanced energy resolution has been demonstrated with such detectors [67].

A diode like configuration of CdTe such as In/CdTe/Pt is a very attractive solution for current mode detectors in high intensity imaging applications because the barrier contact limits the photoconductive gain to unity and prohibits after glow caused by persistent currents which may continue for hundreds of ms or even longer after switching of the X-ray source. After glow is especially a problem in real time imaging as was observed during this work on near ohmic contacted CdZnTe pixel detectors. For example the image of a hole in a metal plate acquired with a CdZnTe pixel detector may stay on as a fading bright spot upon moving the plate to another position if after glow is significant. The photoconductive gain may also cause saturation problems in single frame still imaging if the X-ray intensity is very high.

Barrier contacted CdTe detectors exhibit another problem which may in imaging applications be thought as opposite to after glow. The problem is called polarization and was first observed in high rate counting applications [72]. When detector bias is applied the initially nearly uniform electric field tends to decrease with time in the region near the cathode and is finally localised close to the anode. The polarization effect is generally explained by deep acceptor levels which, when filled with electrons supplied from the cathode, create a negative space charge in the detector bulk [73]. The active detector volume is then decreased which is seen in counting devices as a reduced count rate and in current mode pixel detectors as a weaker image signal. The polarization effect is stronger under radiation and is dependent on the radiation intensity. An object imaged with a real time In/CdTe/Pt pixel detector, e.g., first shows up as a darker region (naturally) in the image but when the object is removed after a few minutes of continuos imaging a ghost image brighter than the background remains in the image. The reason to this is that the polarization in the region under the object is less developed than around the object where the radiation intensity was stronger. After removing the object the detector gives a stronger signal from the region where the object had been.

Polarization can be significantly reduced if not completely eliminated by cooling [73-75]. CdTe detectors with ohmic contacts (Pt/CdTe/Pt) suffer less from polarization [68]. The polarization disappears when the bias is switched off and on again (Publication VII).

A problem related to CdTe monolithic pixel detectors is the technological difficulty to produce patterned indium barrier contacts. The In/CdTe/Pt configuration used in this work allows only the (near) ohmic cathode contact (Pt) to be pixelated. Therefore, the charge integrating pixel amplifiers collect the hole signal. But as shown in sections 5.6 and 6.3 current mode operation is perfectly possible despite the lower mobility of holes because of the long signal integration time.

To improve the energy resolution of spectroscopic detectors signal rise time discrimination [77] and special electrode structures have been introduced. The co-planar grid electrode design is sensitive to the electron signal only and improves significantly the energy resolution [76]. Pixelated detectors yield better energy resolution (measured from individual pixels) than detectors with one electrode covering the whole detector surface. This phenomenon is called the small pixel effect [97] and is due to the fact that single pixels sense signal charge only close to the pixel electrode. The deteriorating effect of the slowly moving and trapped holes which are distributed away from the anode contacts is shared between many pixels and becomes much less significant on single pixels. This is a great benefit for monolithic pixel detectors designed for gamma cameras. The small pixel effect will be evaluated in more detail in section 6.4.

5.2 Pixelisation process

The lithography process developed during this work for monolithic CdTe and CdZnTe pixel detectors is thoroughly described in [78-80] and in [Publication VII]. The CdZnTe crystals used in this work were supplied by eV Products (USA) and the CdTe crystals by Acrorad (Japan).

Initial tests of patterning gold plated CdZnTe detectors revealed the sensitivity of the CdZnTe surface to metal etchants. Patterning small pixels down to a pitch of 35 μm was not a problem as such but if the metal etchant came in touch with the CdZnTe crystal the polished semiconductor surface was destroyed and the surface resistance greatly reduced. In current mode operation the charge signal accumulated on the gate of the input field effect transistor changes the surface voltage of the pixel during the relatively long signal integration time (up to hundreds of ms). The interpixel resistance which is determined by the surface resistivity has to be sufficiently high to prevent signal leakage to neighbouring pixels [Publication VII]. Surface signal leakage tends to smoothen the image by lowering the modulation transfer function and consequently to reduce the spatial resolution.

To protect the CdZnTe surface aluminum nitride (AlN) passivation was applied prior to metal plating or sputtering as described in [Publication VII]. Alternatively a lift off process in which the contact metal is deposited on a patterned layer of photoresist may be be used to avoid the use of etchants. These two alternative processes are shown in figure 5.2. Adequate interpixel resistances of the order of several hundreds of GΩ or more have been achieved both for CdZnTe and depleted CdTe detectors.

For detectors operated in the pulse counting mode the signal integration time is much shorter (0.5 – 1 μs) and hence the surface resistivity requirements less demanding.

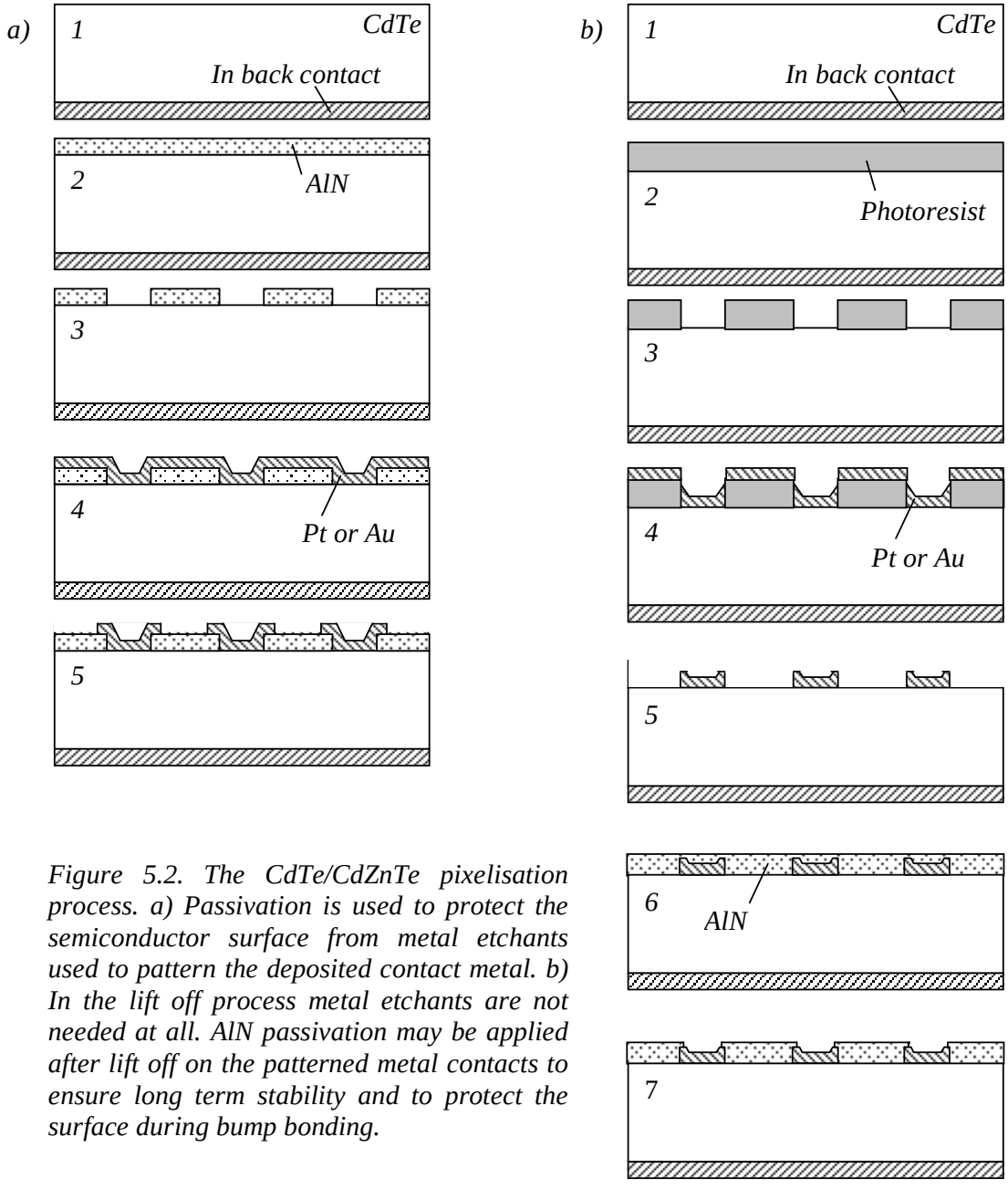


Figure 5.2. The CdTe/CdZnTe pixelisation process. a) Passivation is used to protect the semiconductor surface from metal etchants used to pattern the deposited contact metal. b) In the lift off process metal etchants are not needed at all. AlN passivation may be applied after lift off on the patterned metal contacts to ensure long term stability and to protect the surface during bump bonding.

5.3 Bump bonding

Similar bump bonding processes as used for silicon detectors and described in section 4.2 can be used also for CdTe detectors. Conventional solder bumb bonding cannot be used for CdZnTe since the CdZnTe crystal do not tolerate temperatures much above 120 °C. Heating CdZnTe crystals to higher temperatures was observed to permanently increase the leakage current by several orders of magnitude. Because the wetting temperature of conventional solder bumps is significantly higher than 120 °C a low temperature bump bonding process is necessary for CdZnTe pixel detectors. Indium bump bonding does not include high temperatures but the long term reliability of In bump connections was not found to be satisfactory. A low temperature bumping process based on Pb/Sn/Bi bumps and originally developed at the Technical Research Center of Finland (VTT) [81] was further improved and applied to CdZnTe detectors and also to CdTe detectors [82]. Eventually a lead free Sn/Bi bumping process was developed and applied [119].

Passivation of the pixel detectors is important prior to bump growth and bonding. It was observed that bumps coming into contact with the CdTe/CdZnTe surface as a result of slight misalignment during bump bonding resulted in high currents which showed up in the image as bright spots. The passivation layer prohibits the bumps from touching and damaging the sensitive CdTe/CdZnTe surface.

5.4 Detector and sensor module design and tiling techniques

The layout design of a CdTe pixel detector is shown in figure 5.3. The pixel matrix is extended to the chip edge in order to enable larger mosaic like image areas by side to side mounting of many detectors. Despite the high resistivity edge leakage is still a problem for the outermost pixels and a guard ring may be implemented to collect the edge leakage current. If the guard ring is thin enough the dead space introduced at the edge and between two detectors in a mosaic configuration is insignificant.

The detector thickness is chosen according to the X-ray energy of the target application. For a specific X-ray spectrum N(E) the absorption efficiency η is given by

$$\eta = \frac{\int (1 - e^{-\mu(E)d}) N(E) dE}{\int N(E) dE} \qquad (5.2)$$

where μ is the energy dependent X-ray attenuation coefficient and d the thickness of the detector. The efficiency is plotted against the detector thickness for three different X-ray spectra in figure 5.4. For lower energy spectra high efficiency is reached already at d = 0.5 mm. At d = 1.0 mm the efficiency exceeds 90 % even for the 150 kV spectrum. In gamma imaging when the detector is operated in the counting mode the determination of the optimum detector thickness is more complicated. This is discussed in section 6.4.

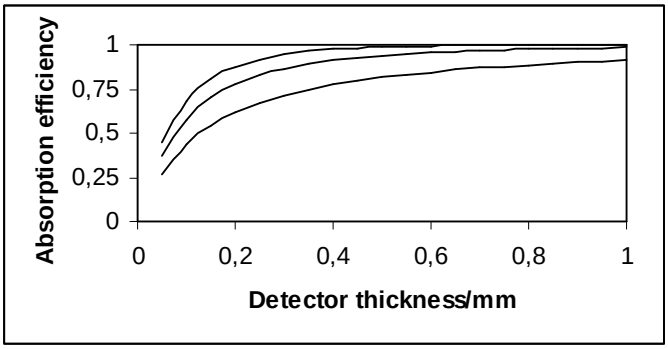


Figure 5.4. Absorption efficiency of a CdTe detector as a function of the detector thickness calculated for three different X-ray spectra (from top to bottom 60 kV, 90 kV and 150 kV, 1 mm Al filtration applied).

The sensor module structure is similar to that of the silicon detectors described in section 4.2. Because one edge of the rectangular sensor module is always needed for signal readout and control wiring a larger image area can consist of a maximum of two sensor rows mounted side by side as shown in figure 5.5. More rows can be added if a special tiling method of mounting the sensor modules in a small angle is applied (figure 5.6). The lifted edge, however, leaves some dead space (see image in section 5.6) and software correction is required to produce a seamless image. In principle the whole chip area of the CdTe/CdZnTe pixel detectors can be made active but in practise software interpolation is required also at the intersection of side to side mounted sensors.

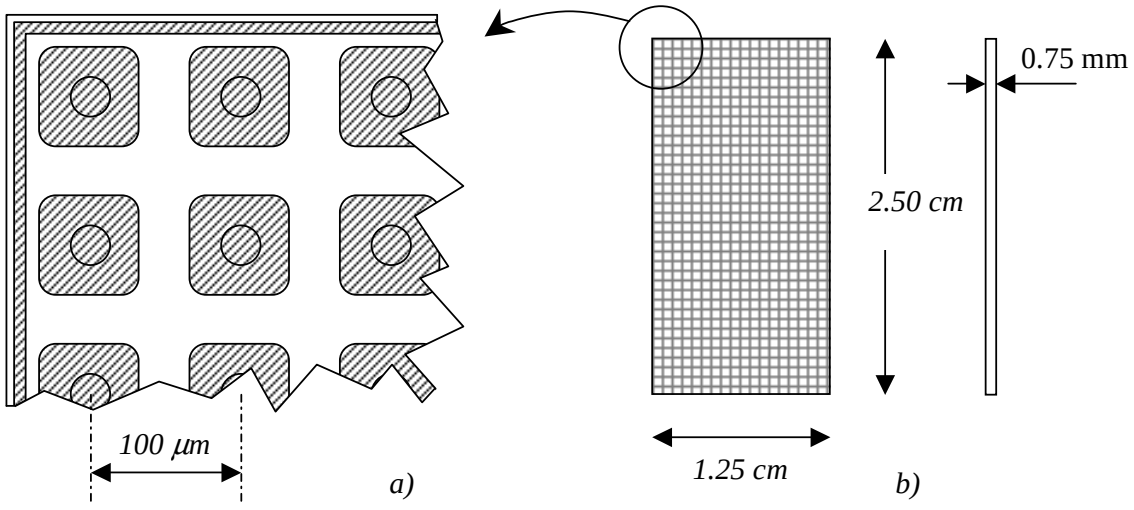


Figure 5.3. CdTe pixel detector design. a) Layout detail showing pixels and the guard ring detector. b) Typical detector dimensions.

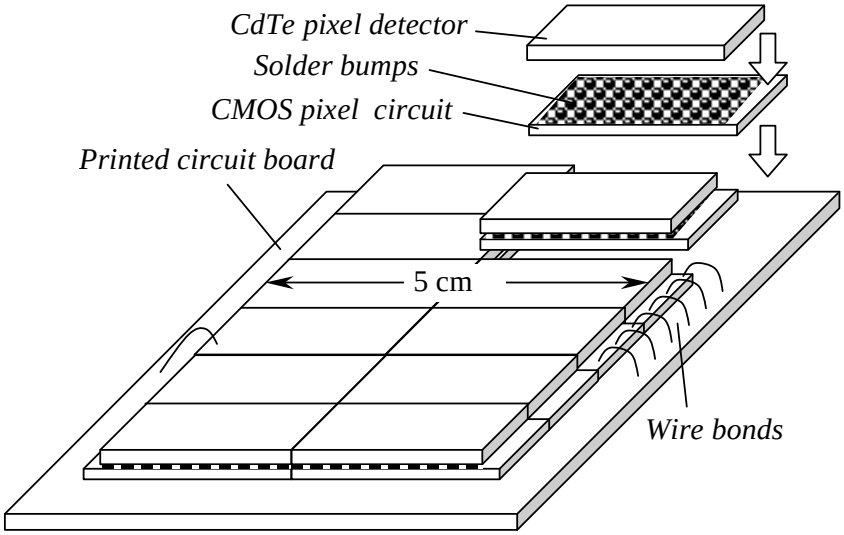


Figure 5.5. Sensor modules mounted sided by side in two rows.

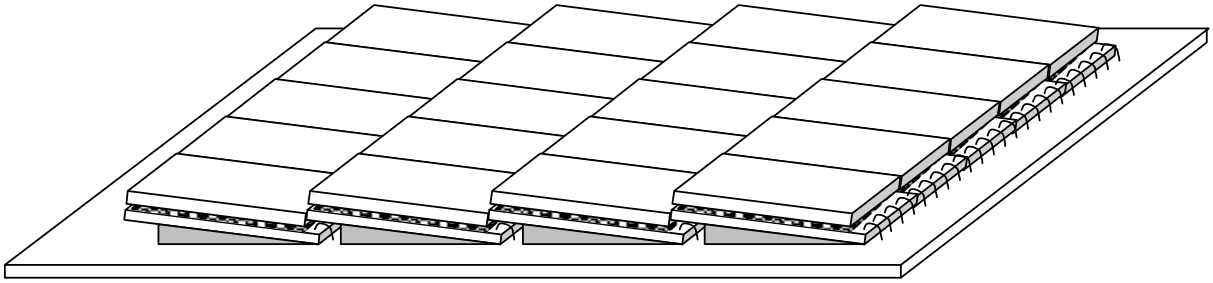


Figure 5.6. Larger mosaic like image area with tilted sensor rows.

5.5 Front end CMOS circuitry

The charge integrating pixel readout circuits developed for the CdTe/CdZnTe detectors of this work are similar to the one used for the silicon pixel detectors (section 4.3). The pixel cell consists of a signal integrating MOSFET, a reset switch and a readout switch (see figure 4.5). For CdZnTe detectors the readout circuit is used in the electron collection mode (negative signal). For the barrier type CdTe pixel detectors the operation is identical to that of the Si detectors.

The surface signal leakage between pixels depends not only on the surface resistance but also on the input capacitance of the charge integrating pixel amplifier. If V is the voltage signal at the input gate, V_1 the voltage around the pixel under consideration as a result of signal leakage, C the

input capacitance, R the interpixel resistance to the pixel neighbourhood and t the signal integration time then [Publication VII]

$$Contrast = \frac{V - V_1}{V + V_1} = \frac{RC}{2t}(1 - e^{-2t/RC}) \tag{5.3}$$

Equation 5.3 describes the signal or contrast loss and is plotted in figure 5.7 as a function of the signal integration time for various time constants RC. Higher input capacitance reduces the contrast loss. On the other hand the sensitivity of the sensor is better if the input capacitance is small. Thus for fast image acquisition applications (short integration time) requiring high sensitivity such as real time imaging or scanning a low input capacitance is preferred. In radiography when the image acquisition time is long (up to several hundreds of ms) and the dose is high the input capacitance has to be large.

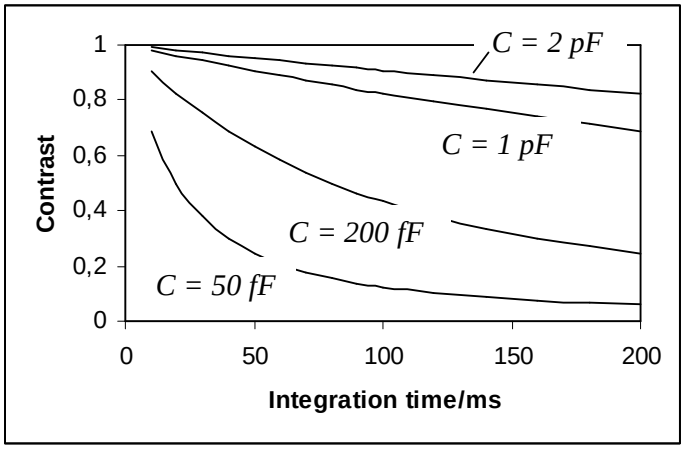


Figure 5.7. Contrast loss caused by interpixel signal leakage as a function of the signal integration time for various values of the input capacitance when the interpixel resistance is 500 GΩ.

Energy dispersive signal recording in the photon counting mode of operation is much more complicated than intensity recording in the current mode. Consequently the pulse counting pixel circuit is also more complex and requires more space [14]. The latest processing technology has, however, enabled energy sensitive signal recording with pixel sizes close to 100 μm [61]. Depending on the application photon counting pixel sensors capable of binary operation (particle physics [14]), up to 18 bit counting (medical imaging [83,84]) and energy spectrum recording (nuclear medicine [25,61]) have been developed. Issues related to photon counting pixel circuits designed for gamma cameras are discussed in sections 5.7 and 6.4.

5.6 Application to real time and dental panoramic X-ray imaging

High sensitivity real time digital X-ray imaging with good spatial resolution is desired both for medical and industrial applications such as fluoroscopy, computerized tomography (CT) and automatic non-destructive testing. In dental panoramic scanning the CdTe sensor technology presented in the previous sections offer some interesting advantages over optically coupled CCD scanning systems.

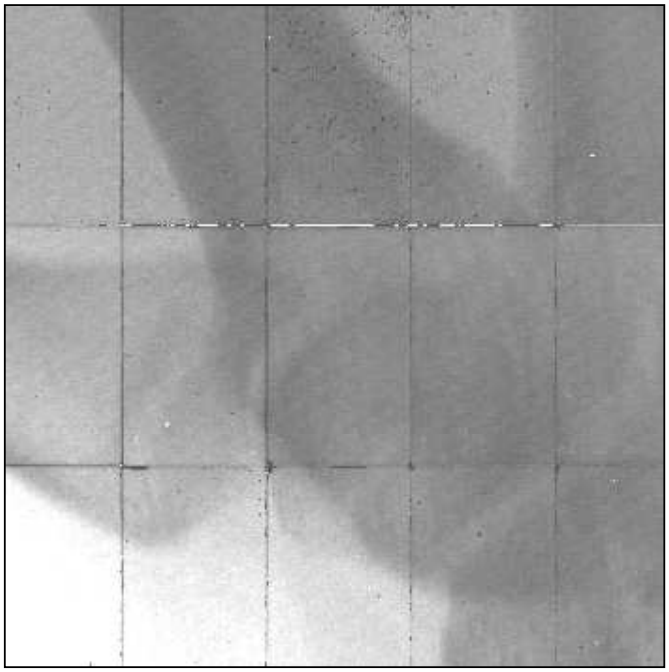


Figure 5.8. An X-ray image of a human hand. The image is acquired with a CdTe mosaic sensor of the design shown in figure 5.6 [85].

General purpose small field (5 cm x 5 cm) prototype real time imagers were built during this work using both of the tiling methods described above.

Figure 5.8 shows one frame of an X-ray video clip of a human hand. This image data was acquired with a sensor constructed with the method of tilted rows [85]. The sensor consists of three rows of detector modules. Each row has five detectors mounted side to side. The dimensions of one detector are 1.80 cm x 1.08 cm. Offset and linear gain correction have been applied before image display but no software interpolation has been used to eliminated the gaps between neighbouring modules.

To reduce the disturbing effect of the sensor module intersections a real time X-ray imager was constructed based on the side to side mosaic technique shown in figure 5.5 [82, Publication VII]. For this sensor larger CdTe pixel detectors of 2.50 cm x 1.25 cm and 2.50 cm x 2.50 cm were processed. Two CMOS readout circuit chips are bump bonded to each one of these larger CdTe detectors. A 5 cm x 5 cm sensor area can then be constructed of four detector modules. The alternative side to side mosaic consists of eight detector modules. A detailed description of these improved real time imagers is given in [Publication VII]. An X-ray image of a ball grid array (BGA) component mounted on a printed circuit board acquired with the four module sensor is shown in figure 5.9. A more sophisticated calibration routine together with software elimination of

the module intersections have been applied [86]. The image is an average of 500 frames collected at a speed of 50 fps.

The quantitative imaging performance of the CdTe real time imagers is discussed in section 6.3.

Panoramic dental X-ray imaging is a method of acquiring a projection view on one image plane of all the teeth of a patient. The method includes scanning of both the X-ray source and the image receiver in such a way that only one layer of the object is displayed sharply [87]. The film speed is adjusted according to the sweep speed of the beam at the layer of interest. Because the beam moves slower along object layers closer to the source and faster along layers closer to the film these layers appear blurred in the final image.

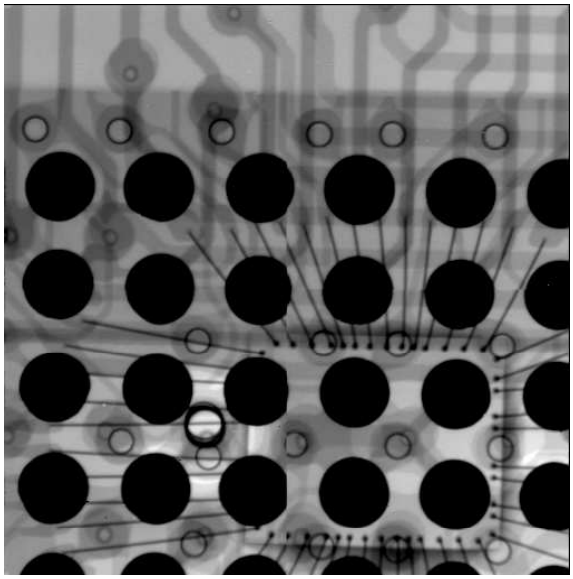


Figure 5.9. An X-ray image of a BGA component acquired with a 4 module CdTe real time imager. The image is an average of 500 frames collected at 50 fps when the X-ray tube voltage was 70 kV, the tube current 40 μA and the source to sensor distance 50 cm. Image magnification is applied by reduced source to object distance [82].

Digital dental panoramic systems based on optically coupled CCDs are commercially available [88]. To achieve maximum scanning speed the signal readout of the CCDs is performed in the time delayed integration (TDI) mode. In the TDI mode the signal charge collected in the CCD wells is transferred in the opposite direction to the scan movement along the columns vertical to the scan direction. The clock frequency is adjusted to the scan speed so that the signal integration time of one pixel between two transfers is equal to the time elapsed for the CCD to move one pixel width. The charge signals accumulated in the last row which are read out with high speed are thus the sum of the pixel signals in each column and corresponds to one row in the final image. The TDI mode optimises the scan speed and eliminates any dead time in the CCD readout. A CCD TDI scanner is similar to the X-ray film from the image acquisition point of view, i.e., the produced image exhibits sharply only one object layer. All other object layers are lost.

The CMOS-CdTe pixel detectors offer two important advantages over the CCD systems. Firstly the X-ray absorption efficiency of CdTe is higher by a factor of approximately two than that of the scintillators used in the CCD systems. This allows faster scanning or better signal to noise ratio (SNR) at equal scanning speed. Secondly, while the CCD signal charge collecting elements are

also used for signal readout the charge signal accumulated at the input gates of the CMOS pixel circuits are possible to be read out independently of the signal integration. Fast image frame acquisition is thus possible without a TDI like readout mode. With the CMOS-CdTe pixel detector image frames are collected faster than the scanning speed and these frames can then be added in any desired combination to reconstruct not only one but several object layers either as projections or as a 3D image of the object.

Figure 5.10 shows a photograph of a prototype CdTe X-ray image scanner which consists of three pixel sensor modules mounted side to side. The pixel size is 100 μm and the number of pixels of one detector is 180 x 108 = 19440. The active length of the scanner is 5.4 cm. Figure 5.11 shows a panoramic projection image of a skull phantom acquired with this CdTe sensor [85].

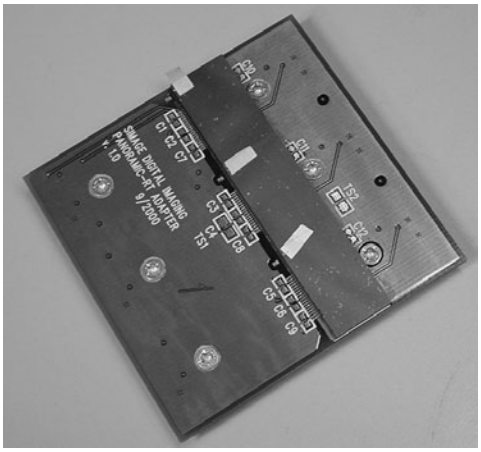
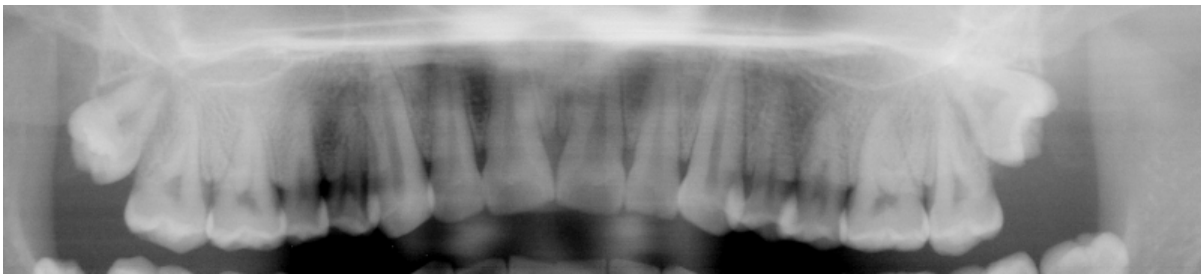


Figure 5.10. A prototype CdTe X-ray scanner for panoramic dental imaging [85].

Figure 5.11. A panoramic projection image of a skull phantom (real human teeth) acquired with a CdTe X-ray scanner [85].



Further development of the CMOS-CdTe scanning imager [82] resulted in a full size product level panoramic X-ray camera. The camera utilizes both of the special advantages of the CMOS-CdTe technology as described above. The camera which is shown in figure 5.12. exhibits excellent image quality (figure 5.13) and offers an auto focus function based on the frame reconstruction feature for correction of faulty patient positioning [120].

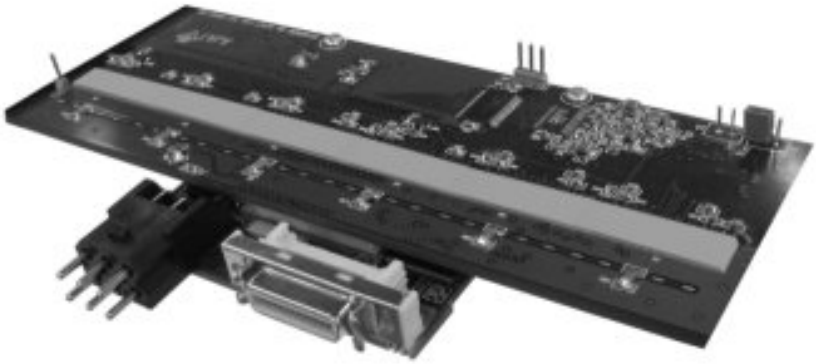


Figure 5.12. A full size CMOS-CdTe panoramic camera [82].



Figure 5.13. A panoramic projection image of a human skull acquired by the Ajat CMOS-CdTe panoramic camera [82].

5.7 Gamma imaging

In gamma imaging the concentration distribution of a radioactive tracer is measured with a position sensitive gamma detector. Perhaps the most important use of gamma imaging is in nuclear medicine [89] but gamma labeled tracers are also used in industrial applications such as in investigation of the distribution of the lubricating oil in car engines.

In nuclear medicine the distribution of the gamma emitting tracer is conventionally measured with a photon counting Anger or gamma camera [90]. The Anger camera consists of photomultiplier (PM) tubes connected to a sodium iodide (NaI) scintillator. To acquire an image of

the tracer distribution and to reduce the noise produced by Compton scattered rays a collimator is used in front of the scintillator plate. In gamma imaging both the position and the energy information of the recorded photons are important. The energy information is used to discriminate Compton scattered rays and thus to improve the image SNR. In addition to good spatial resolution low single event noise and consequent high energy resolution is, therefore, also desired for efficient Compton rejection.

The intrinsic spatial resolution of conventional gamma cameras is about 3 mm [25,90]. The energy resolution is also relatively poor being at best 10 % [25] or 14 keV FWHM for the most commonly used label ^{99m}Tc which emittes 140 keV gamma rays. To achieve sub millimetre position resolution and to improve Compton rejection CdTe and CdZnTe pixel detectors have been developed to substitute the scintillator connected PM tubes [55,60,61].

Publication VIII describes the CdTe gamma camera developed by Oy Ajat Ltd. and analysed in this work.

In addition to the hole trapping problem in CdTe/CdZnTe detectors the effect of the signal charge carrier diffusion (which is common to all semiconductor detectors) influences the imaging performance of photon counting CdTe/CdZnTe gamma cameras. At small pixel sizes (< 1 mm) the signal charge sharing between pixels due to carrier diffusion becomes significant reducing the photo peak efficiency and eventually limiting the pixel size. In low intensity applications it is possible to compensate the signal charge spread by adding the signal of neighbouring pixels to the center pixel signal [61] but at higher intensities and for large pixel arrays recording the analog signal from each pixel separately is no longer feasible. In such applications a signal readout configuration with a digital counter at each pixel is preferred. The counter stores the number of hits above the discrimination level.

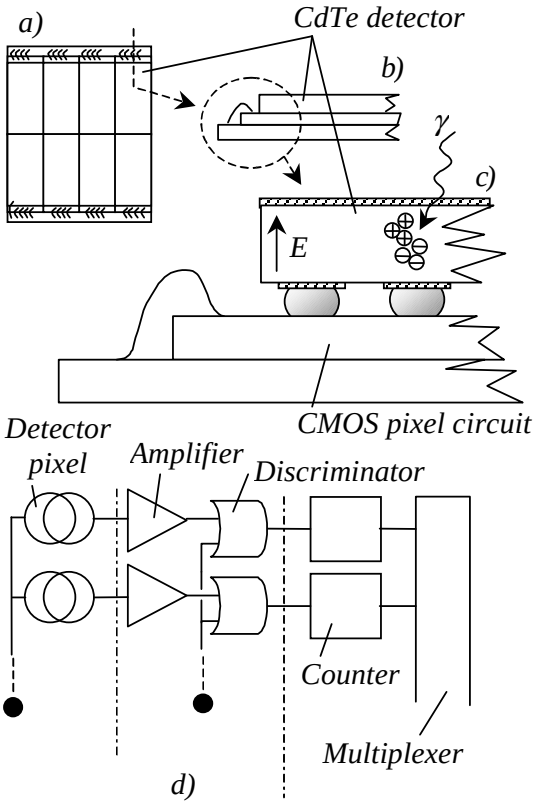


Figure 5.14. Schematic view of a CdTe gamma camera. a) Top view of the sensor. b) and c) Cross section of one detector. d) Pixel electronics. All pixels are connected to a common multiplexer.

A schematic view of a CdTe gamma camera with pixel level counting is shown in figure 5.14 [82, Publication VIII]. The effect of the pixel size and detector thickness on the photo peak efficiency of a gamma camera of this type is discussed in section 6.4.

6. Performance analysis

6.1 Definitions and methods

The detective quantum efficiency or DQE is generally regarded as the most useful measure of performance of an imaging system. The DQE can be understood as the fraction of the number of quanta entering the imaging system effectively used by the system to produce an image. The DQE as a function of the spatial frequency of the object details is defined as

$$DQE(f) = \frac{SNR_{out}^2}{SNR_{in}^2} = \frac{\bar{S}^2 MTF^2(f)}{\Phi NPS(f)} \tag{6.1}$$

where SNR_{in} and SNR_{out} are the signal to noise ratios of the quantum field at the detector input and of the image at the detector output, respectively. S is the average image signal, Φ is the entering X-ray fluence, MTF is the modulation transfer function of the imaging system and NPS is the noise power spectrum of the image.

The MTF describes the signal attenuation as a function of the spatial frequency and is defined as the modulus of the Fourier transform of the line spread function or as

$$MTF(f) = \left|F\left[LSF(x)\right]\right| = \left|\frac{1}{\sqrt{2\pi}} \int_{-\infty}^{\infty} LSF(x) e^{i2\pi fx} dx\right| \tag{6.2}$$

The MTF is always scaled to unity at f = 0. The line spread function LSF is the system response to a delta stimulus. When evaluating digital imaging systems which sample the image signal at discrete pixels the definition 6.2 is replaced by the discrete MTF. The digital representation of the MTF is

$$MTF_{dig}(f) = \frac{1}{N}\left|\sum_{k=0}^{N-1} LSF(x_k) e^{i2\pi f x_k}\right| \tag{6.3}$$

Here $LSF(x_k)$ is the value of the line spread function at the k^{th} pixel. The noise power spectrum NPS is defined as

$$NPS(u,v) = \lim_{X,Y\to\infty} \frac{1}{XY} E\left\{ \left| \iint_{XY} \sigma(x,y) e^{-2\pi i(ux+vy)} dxdy \right|^2 \right\} \tag{6.4}$$

and describes the noise frequency component distribution in the image area XY. In equation 6.4 σ(x,y) is the difference between the average image signal and the signal at point (x,y) and E stands for expectation value, i.e., average. The one dimensional digital representation of the NPS is

$$NPS_{dig}(u) = \frac{A_{pix}}{N_x N_y} \frac{1}{M} \sum_{i=0}^{M-1} \left\{ \left| DFT\left(\sum_{n_y=0}^{N_y-1} \sigma_{n_x n_y} \right) \right|^2 \right\} \tag{6.5}$$

The NPS_{dig} in equation 6.5 is thus the average discrete Fourier transform of the average signal variation in the x direction scaled by the pixel size and the number of pixels under consideration.

The theoretical maximum DQE at zero spatial frequency is limited by the X-ray absorption efficency of the detector material (see section 3.3). The DQE(0) can never exceed the absorption efficience η as given by equation 5.2:

$$DQE(0) \le \eta \tag{6.6}$$

The theoretical limit of the MTF is determined by the pixel size of the imaging sensor. Since the sharpest response of the imaging system to a delta stimulus is as wide as one pixel the maximum MTF is the Fourier transform of a step function with a width of one pixel:

$$MTF_{\max}(f) = \frac{1}{a} \left| \int_{-a/2}^{a/2} e^{i2\pi fx} dx \right| = \frac{\sin \pi fa}{\pi fa} \tag{6.7}$$

when a is the pixel width. Then by combining equations 6.1, 6.6 and 6.7 we may write the theoretical maximum frequency dependent DQE as

$$DQE_{\max}(f) = \eta \frac{\sin^2 \pi fa}{(\pi fa)^2} \tag{6.8}$$

Equation 6.8 is true for an imaging system operating in the pulse counting mode. As explained in section 3.3 current mode operation yields a maximum DQE that is always less than DQE_{max} of equation 6.8.

The dynamic range is defined as the ratio of the maximum acquirable signal before saturation to the smallest detectable signal [19] or as

$$DR = \frac{S_{\max}}{S_{\min}} \tag{6.9}$$

The contrast resolution depends on the dynamic range. Recalling the definition of the contrast given in equation 3.13 and using $S_{min} = S_0 - S$ and $S_{max} = S_0$ we can write for the lowest detectable contrast (by combining equations 3.13 and 6.9)

$$C_{\min} = \frac{1}{2 \cdot DR - 1} \approx \frac{1}{2 \cdot DR} \tag{6.10}$$

X-ray film has a dynamic range of 50 – 100 which means that the contrast resolution is approximately 1 %. Digital sensors have generally a much higher intrinsic dynamic range (up to several thousands). However, the minimum detectable signal is in practice most often defined by the quantum noise which equals the square root of the maximum signal possible to acquire before saturation. Thus, if the signal in X-rays at saturation is N the dynamic range equals $\sqrt{N}$.

In order to measure the DQE the X-ray fluence entering the imaging device has to be known accurately and both the NPS and the MTF have to be determined as a function of the spatial frequency from the acquired image data.

The X-ray fluence can in principal be calculated theoretically from the energy spectrum of the output of the X-ray tube taking into account possible beam hardening by any filters between the tube and the X-ray sensor. If I is the tube current, t the exposure time and $N_0(E)$ the filtered energy spectrum leaving the tube in X-ray quanta/unit area, time and tube current then the total number of photons/area or the fluence at the detector input is

$$\Phi = It \int_0^{E_{\max}} N_0(E) e^{-\mu_{air}(E)h} dE \tag{6.11}$$

where $\mu_{air}(E)$ is the total energy dependent attenuation coefficient of air and h is the distance between the tube and the sensor surface. In practice, however, it is often difficult to know accurately I and t and sometimes h and, therefore, the X-ray exposure should be measured at the detector surface if an accurate fluence estimation is required. If X is the measured exposure in Roentgens by an air ionization chamber and $\mu_{en,air}(E)$ is the energy attenuation coefficient of air then the photon fluence per unit exposure for the entire X-ray spectrum is

$$\frac{\Phi}{X} = \frac{\int_0^{E_{max}} N(E)dE}{\int_0^{E_{max}} N(E)\frac{\mu_{en,air}(E)}{\rho_{air}} \cdot \frac{1C/kg}{33.8J/kg} \cdot \frac{1R}{2.58 \cdot 10^{-4} C/kg} \cdot E \cdot 1.6022 \cdot 10^{-19} J/eV} \qquad (6.12)$$

where N(E) is the normalised energy spectrum generally calculated with X-ray spectrum simulators. In this work the X-ray fluence Φ was determined by measuring the X-ray exposure at the detector surface with a Keithley 35050A dosimeter and applying equation 6.12.

In this work for all sensors tested the NPS was calculated according to equation 6.5 from the image under consideration by dividing the image into 16 regions of equal area and by averaging the 16 acquired individual NPS of each area.

The spatial resolution of imaging systems is usually described by the so called presampled MTF (preMTF) [93]. The preMTF includes the effect of the sampling aperture defined by the pixel size but not the effect of the process of sampling. The response of the sensor to a thin slit stimulation, e.g., depends on the relative position of the slit to the pixel columns. If the slit is aligned to the pixel columns and placed exactly above the intersection of two columns the response is different than if the slit is on top of the center of one pixel column. This effect of aliasing has to be taken into account when determining the MTF.

The MTF is measured by imaging either a thin slit or a sharp edge placed on top of the sensor surface. The slit response as such or the derivative of the edge response is used in equation 6.3 as the LSF. To obtain the preMTF the slit has to be clearly thinner than the pixel width, aligned to the columns and placed exactly on top of one column. Similarly the edge has to be very sharp and aligned exactly along one column intersection to produce the preMTF. Since accurate aligning of a slit or edge is difficult a more practical method of sub pixel sampling (over sampling) is usually preferred [94]. This method includes positioning the slit or edge across the sensor pixel rows in a small angle to the pixel columns. The reconstruction of the sensor response function is then

performed by combining the different responses of several rows as illustrated in figure 6.1 (figure 6.1c). This method yields the preMTF which in the ideal case is the sinc function of equation 6.7.

An alternative method to determine the MTF is to average the response of all the rows to produce the average response function (figure 6.1d). However, the derivative of the average edge response function applied as the LSF to equation 6.3 does not yield the preMTF but an MTF which includes sampling effects. Typically, if enough rows are included in the average, this method gives a rather conservative MTF corresponding to a "worst case" edge response shown in figure 6.1d.

In this work the edge method together with the average sampling method was used in the determination of the MTF. While the sub pixel sampling method requires a high image signal to noise ratio to obtain a smooth LSF the average sampling method is immune to image noise and the edge image can be acquired more easily even with low dose. It can also be argued that the MTF obtained with the average sampling method is more realistic than the preMTF in describing the response of the imaging system.

The MTF result obtained with the edge method depends also to some extent on the definition of the discrete derivation of the LSF. In this work the derivative was defined as

$$y_i = \frac{1}{2dt}(x_{i+1} - x_{i-1}) \qquad (6.13)$$

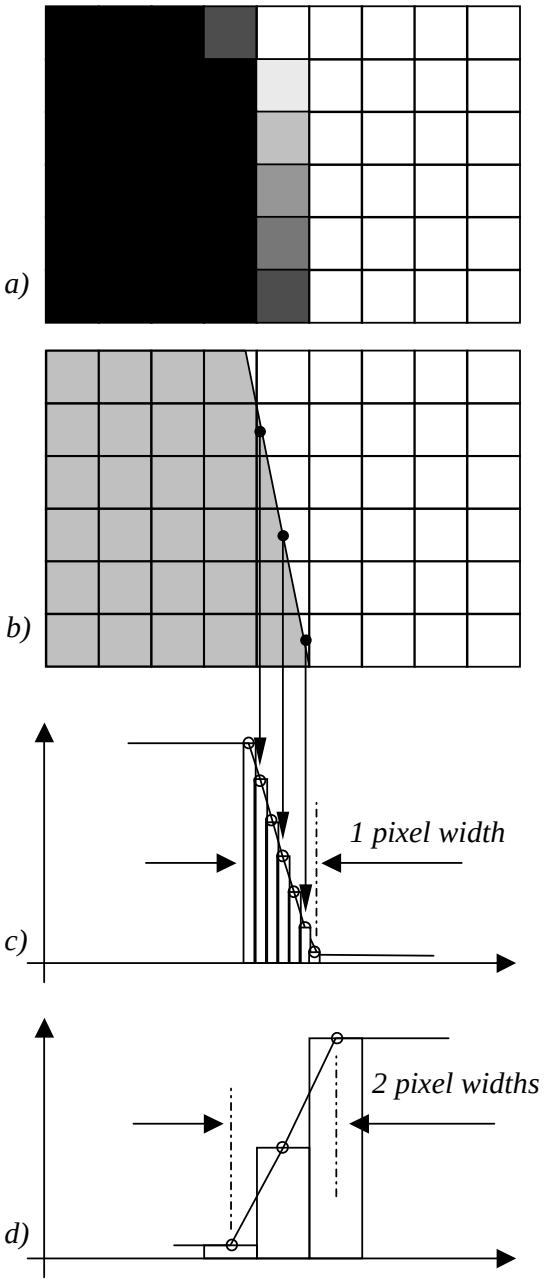


Figure 6.1. Illustration of the sub pixel sampling method to reconstruct the edge response function in comparison to the averaging method. a) Ideal image of a sharp edge. b) Position of the edge crossing the pixel rows. c) The finely sampled edge response function according to the sub pixel sampling method. d) The average edge response function.

when x_i and y_i are the average image signal and the average LSF value at the i^{th} pixel, respectively, and dt is the sampling interval defined by the pixel size.

The ideal MTF determined with the average sampling method is lower than the sinc function. This is illustrated in figure 6.2 which shows the ideal MTF of the average sampling method in comparison to the sinc function for a pixel size of 100 μm.

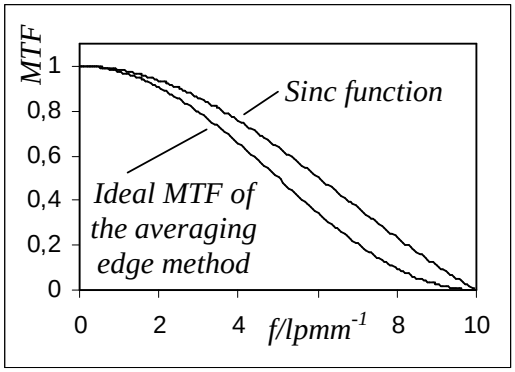


Figure 6.2. The ideal MTF calculated with the averaging edge method for a pixel size of 100 μm. The ideal average edge response function is shown in figure 6.1d.

6.2 Performance of the silicon intra oral imaging sensor

The performance of the intra oral sensor in terms of SNR, MTF and DQE is presented in [Publication V]. Some supplementary issues are discussed here.

The MTF curve is presented in [Publication V] in comparison to the sinc function. As mentioned in section 6.1 the averaging edge method actually yields an ideal maximum MTF somewhat lower than the sinc function. Therefore, it is more appropriate to compare the measured MTF to this maximum as is done in figure 6.3. The intra oral MTF follows very closely the ideal MTF (the small difference can be explained by the fairly large focal spot of the X-ray tube used in the measurements as pointed out in [Publication V]) and thus the spatial resolution is defined by the pixel size. The 14 lp/mm grid of a line pair phantom

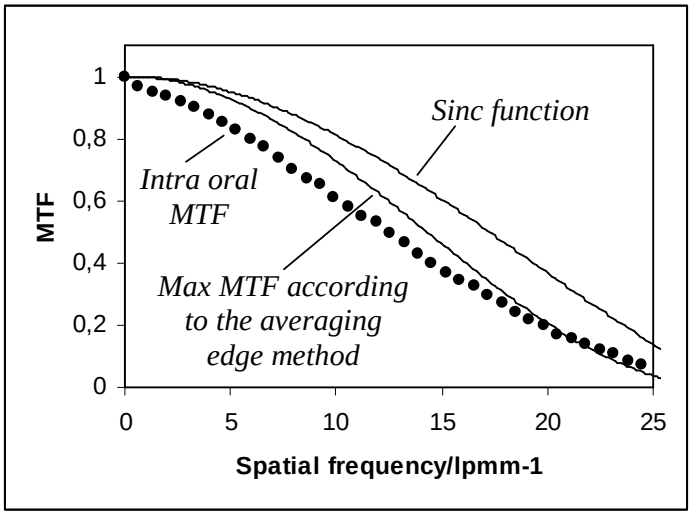


Figure 6.3. The intra oral MTF in comparison to the theoretical maximum MTF calculated from the ideal edge response.

is clearly visible in an X-ray image shown in [Publication V] (the Nyquist frequency for 35 μm pixels is 14.3 lp/mm). This supports the MTF result.

Because of the possibility to acquire multiple data frames without inactive time the dynamic range of the intra oral sensor is in principal unlimited. The dynamic range of one frame is, however, of interest since the maximum X-ray intensity is determined by the frame readout speed and by the effective signal storage capacity of the input MOSFET. The storage capacity depends on the gate capacitance, on the width of the linear region of the FET and on the detector dark current.

The input capacitance is designed to C_g = 1.3 pF and the linear range of the transistor extends from a gate voltage V_g of 1.9 V to 3.9 V. Thus the total capacity is $Q = C_g V_g = 2.6 \cdot 10^{-12}$ C = $16 \cdot 10^6$ electrons. The pixel leakage current of a good detector is typically at most 0.1 pA. At a normal frame readout speed of 5 MHz the integration time is approximately 170 ms (the number of pixels is 835584). Then the average dark signal is $Q_{dark} = 1.7 \cdot 10^{-14}$ C = $0.1 \cdot 10^6$ electrons which is insignificant compared to the total capacity. Due to the long charge integration time the dominant noise source at the front end is the detector dark current. The dark current noise is given by

$$\delta q = \sqrt{2eIt} \tag{6.14}$$

where e is the elementary charge, I the dark current and t the integration time. In our case δq = 460 electrons. Using the definition of equation 6.9 for the dynamic range we get DR ≈ 35000. Thus we



Figure 6.4. An X-ray image of a mouse acquired with the intra oral sensor [96].

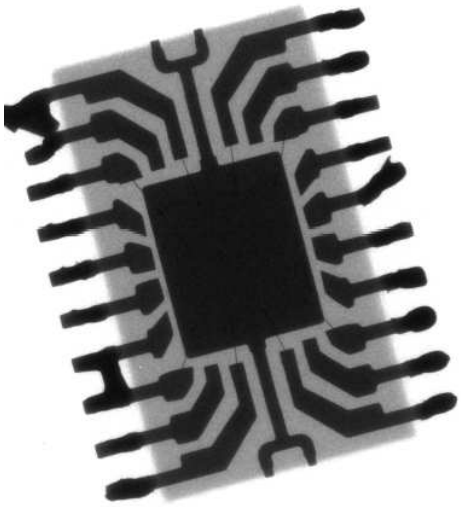


Figure 6.5. An X-ray image of an encapsulated integrated circuit acquired with the intra oral sensor. Bond wires are visible.

see that the intrinsic dynamic range is limited not by the front end CMOS but by the 12 bit A/D converter used which has a noise of about 1 – 2 ADC counts. Limited by the A/D converter the DR ≈ 2000 – 4000. In silicon one X-ray of 30 keV (average energy in dental imaging) creates 30000 eV/3.6 eV = 8300 signal carrier pairs. Approximately 2000 X-rays of 30 keV can then be acquired in one data frame. The intra oral sensor with the current 12 bit A/D converter should hence be almost single photon sensitive. However, measurements show that the sensor is quantum limited only above a dose of 500 μGy [Publication V]. This corresponds to an equivalent noise of about 40 X-rays and limits the single frame dynamic range to about 100. The source of this additional noise is not clear but it may be related to insufficient shielding of the encapsulation which allows disturbances from the X-ray tube to enter the sensor.

In addition to the images shown in section 4.5 and in [Publication V] the high spatial and contrast resolution of the intra oral sensor are demonstrated in figures 6.4 and 6.5.

6.3 Performance of the CdTe real time imager

The DQE(0) of CdZnTe detectors with a pixel size of 35 μm was measured to be close to

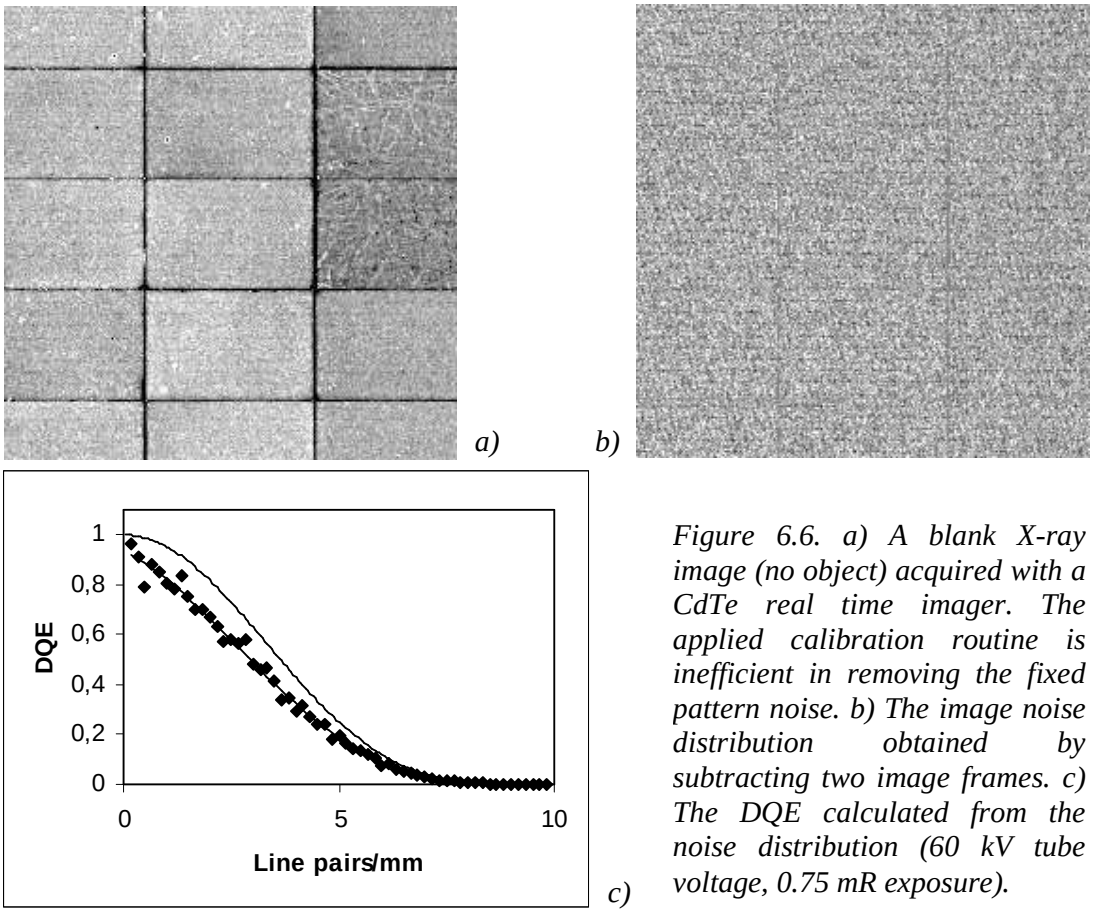


Figure 6.6. a) A blank X-ray image (no object) acquired with a CdTe real time imager. The applied calibration routine is inefficient in removing the fixed pattern noise. b) The image noise distribution obtained by subtracting two image frames. c) The DQE calculated from the noise distribution (60 kV tube voltage, 0.75 mR exposure).

100 % for X-ray spectra generated with 60 kV and 80 kV tube voltages [Publication IV]. These results were obtained by monitoring the fluctuations of individual pixels at repeated exposures. Due to crystal non-uniformity problems the CdZnTe detectors were never used to built larger area mosaic like sensors.

The DQE of the real time imagers built of CdTe detectors was studied first on a sensor of the tilted rows mosaic design explained in section 5.4. An X-ray image acquired with this sensor is shown in figure 5.8. When this sensor was tested an efficient calibration routine for the CdTe real time imagers had not yet been developed. Therefore, the DQE was determined from data with fixed pattern noise removed by subtraction of two image frames. An acquired raw white image frame (60 kV tube voltage, 1 mm Al filtration) and the corresponding subtracted image are shown in figure 6.6.

The average DQE shown in figure 6.6c is calculated from the subtracted image. With the DQE curve following very closely the ideal curve this result shows the great potential of CdTe as a detector material for digital X-ray imaging.

The improved CdTe real time imager introduced in section 5.6 and described in detail in [Publication VII] exhibit a high DQE even without image frame subtraction. The real time calibration applied now [86] efficiently removes the fixed pattern noise. MTF, SNR and DQE results for this sensor are shown in [Publication VII] and are not repeated here.



Figure 6.7. A single frame X-ray image of a Japanese coin acquired with the CdTe real time imager [82].

To enable real time imaging at high frame rates and low exposures the sensitivity of the CdTe imager reported in [Publication VII] is enhanced by minimising the input capacitance to 50 fF. The sensor is single X-ray sensitive. At 60 keV the storage capacity is approximately 50 X-rays and thus according to equation 6.10 the single frame contrast resolution is about 1 %. Unlimited contrast resolution is possible by averaging subsequent frames as long as the X-ray intensity is low enough not to saturate single frames. The single frame contrast resolution is demonstrated in figure 6.7.

6.4 Simulated photo peak efficiency of CdTe and CdZnTe gamma cameras

In medical gamma camera imaging a threshold energy is used in the signal recording circuit in order to discriminate compton scattered gamma rays which do not carry image information. True signals which suffer from charge loss will then also be discriminated reducing the number of recorded gamma counts and thus the detector efficiency. As mentioned in section 5.7 signal charge loss in CdTe and CdZnTe detectors are due to carrier trapping and diffusion. A CdTe/CdZnTe gamma camera designed for high intensity imaging according to the description in section 5.7 and [Publication VIII] will suffer from reduced efficiency depending on the semiconductor material properties (carrier life time and mobility), the detector thickness, electric field strength and pixel size.

The photo peak efficiency is defined here as the ratio of the number of recorded gamma counts/pixel above the discrimination level to the number of gamma photons/pixel entering the detector. We may call this the effective gamma absorption efficiency η_{eff} and write

$$\eta_{eff} = \eta\gamma \tag{6.15}$$

when η is the absorption efficiency of the detector and γ is the ratio of the recorded gammas to the absorbed gammas. If the detector is quantum limited, i.e., if the dominant noise source is the quantum noise then η_{eff} equals the zero frequency DQE.

To calculate η_{eff} as a function of the detector thickness, bias voltage and pixel size we extend the physical model presented in [97] and [98] to take into account also the lateral spread of the drifting signal charge cloud. The aim is to find the optimum detector thickness which gives the highest η_{eff} and to determine the limiting pixel size still yielding an adequate η_{eff}. We also want to compare the perfomance of CdTe detectors to that of CdZnTe detectors.

6.4.1 Physical model

Following a gamma ray interaction in a semiconductor pixel detector a signal charge is accumulated at the amplifier input which is connected to the detector pixel anode. The charge signal is induced mainly by the moving electrons which eventually arrive at the pixel contact but is also affected by the trapped electrons and by the positive holes, both moving and trapped. The induced charge signal can be calculated from the theory of electrostatics using the so called image charge

method [97]. Assuming zero charge injection from the detector electrodes a point charge q located at (x, y, z) in the detector bulk according to figure 6.8 will induce a surface charge at the location (x_p, y_p) of the plane $z = z_p = 0$ equal to

$$\sigma(x_p, y_p) = -\frac{q}{4\pi}\sum_{k=-\infty}^{\infty}\left[\frac{2kL+z}{((x_p-x)^2+(y_p-y)^2+(2kL+z)^2)^{3/2}} - \frac{2kL-z}{((x_p-x)^2+(y_p-y)^2+(2kL-z)^2)^{3/2}}\right] = -\frac{q}{4\pi}\sum_{k=-\infty}^{\infty}G_k \qquad (6.16)$$

where L is the detector thickness and the index p refers to the pixel electrode plane. The total charge signal induced on the pixel by the point charge is calculated by integrating equation 6.16 over the area of the pixel electrode:

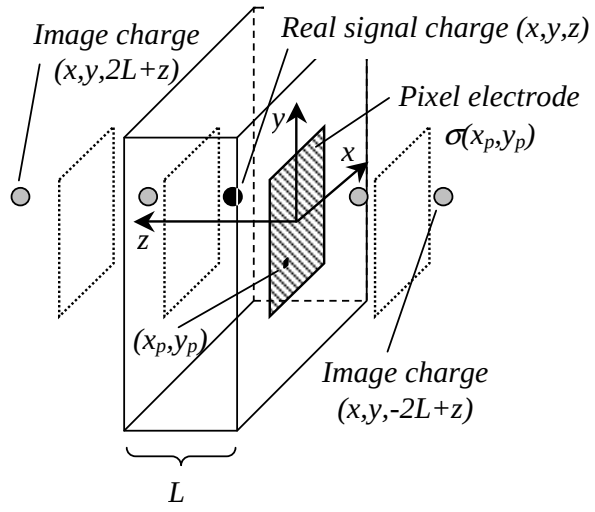


Figure 6.8. Illustration of the image charge method applied to a detector of thickness L.

$$Q_{signal} = \iint_{pixel}\sigma(x_p, y_p)dx_p dy_p \qquad (6.17)$$

The charge appearing in the detector volume after a gamma interaction is not a point charge but a charge distribution depending on the charge carrier life time, the diffusion constant and the electric repulsion between the carriers. Figure 6.9 illustrates the charge distribution at time t elapsed from the moment of the gamma interaction.

The lateral and vertical spread of the moving signal charge can be estimated by solving the three dimensional diffusion equation [53,99]

$$\frac{\partial\rho(x,y,z,t)}{\partial t} = eN_0 D\left(\frac{\partial^2\rho}{\partial x^2}+\frac{\partial^2\rho}{\partial y^2}+\frac{\partial^2\rho}{\partial z^2}\right) \qquad (6.18)$$

Here e is the elementary charge, D the diffusion constant and N_0 is the number of charge carriers

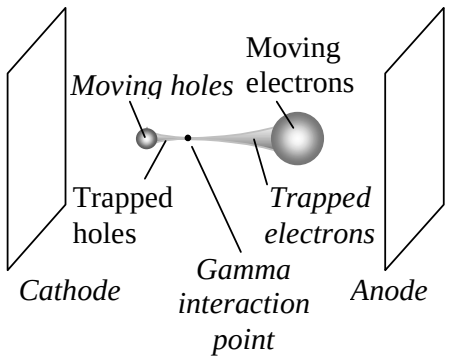


Figure 6.9. Charge distribution in the detector volume following a gamma interaction

induced by the gamma ray. The diffusion constant is given by the Einstein relation as [99]

$$D = \frac{kT}{e}\mu \qquad (6.19)$$

when k is the Boltzmann constant, T the absolute temperature and μ the carrier mobility. In addition to the diffusion the electric repulsion between the drifting charge carriers should also be taken into account in the calculation of the spread of the signal charge cloud. However, as predicted in [100] the electric repulsion is not very significant compared to the diffusion effect when the number of carriers is below a few tens of thousand. We are interested in signals produced by 140 keV gamma rays emitted by the ^{99m}Tc isotope. The average number of carriers created by a 140 keV gamma photon in CdTe is 140,000 eV/4.43 eV = 31,600 and in CdZnTe 140,000 eV/5.0 eV = 28,000. Therefore, we omit the effect of electric repulsion between the carriers and describe the spread of the signal charge cloud simply with equation 6.18.

The solution of equation 6.18 is a gaussian distribution of the form

$$\rho(x,y,z,t) = eN_0 A t^{-(3/2)} e^{-(x^2+y^2+z^2)/Bt} \qquad (6.20)$$

where A and B are constants which can be solved by substituting equation 6.20 into equation 6.18 and by using

$$\int_0^\infty e^{-x^2/2}dx = \sqrt{\frac{\pi}{2}} \qquad (6.21)$$

The result is

$$\rho(x,y,z,t) = \frac{eN_0}{(4\pi Dt)^{3/2}} e^{-(x^2+y^2+z^2)/4Dt} \qquad (6.22)$$

Due to charge trapping the total number of moving charge carriers decreases with time according to

$$N(t) = N_0 e^{-t/\tau} \qquad (6.23)$$

where τ is the carrier life time. Since an electric field E = V/L is applied over the detector volume (V is the applied voltage and L the detector thickness), the signal charge cloud moves along the z-axis with a speed v = μE where μ is the charge carrier mobility (we assume that the electric field is constant over the complete detector volume). Thus we have to write the moving charge distribution as

$$\rho(x,y,z,t) = \frac{eN_0}{(4\pi Dt)^{3/2}} e^{-t/\tau} e^{-(x^2+y^2+(z+vt)^2)/4Dt} \tag{6.24}$$

The trapped charge during an infinitely short time dt can be deduced as (using $e^x = 1 + x + x^2/2! + \ldots \approx 1 + x$)

$$d\rho = \rho(x,y,z,t)(1-e^{-dt/\tau}) = \frac{dt}{\tau}\rho(x,y,z,t) \tag{6.25}$$

Combining equations 6.24 and 6.25 we get

$$d\rho = \frac{eN_0}{(4\pi Dt)^{3/2}} \frac{1}{\tau} e^{-t/\tau} e^{-(x^2+y^2+(z+vt)^2)/4Dt} dt \tag{6.26}$$

We may now consider a gamma ray interaction at the point (x_0, y_0, z_0) in the detector bulk at time t = 0 and write the charge distributions at an elapsed time t for both the trapped and the moving electrons and holes as

$$\begin{aligned}
\rho_{e,moving} &= -\frac{eN_0}{(4\pi D_e t)^{3/2}} e^{-t/\tau_e} e^{-((x-x_0)^2+(y-y_0)^2+(z-z_0+v_e t)^2)/4D_e t} \\
\rho_{e,trapped} &= -\int_0^t \frac{eN_0}{(4\pi D_e t')^{3/2}} \frac{1}{\tau_e} e^{-t'/\tau_e} e^{-((x-x_0)^2+(y-y_0)^2+(z-z_0+v_e t')^2)/4D_e t'} dt' \\
\rho_{h,moving} &= \frac{eN_0}{(4\pi D_h t)^{3/2}} e^{-t/\tau_h} e^{-((x-x_0)^2+(y-y_0)^2+(z-z_0-v_h t)^2)/4D_h t} \\
\rho_{h,trapped} &= \int_0^t \frac{eN_0}{(4\pi D_h t')^{3/2}} \frac{1}{\tau_h} e^{-t'/\tau_h} e^{-((x-x_0)^2+(y-y_0)^2+(z-z_0-v_h t')^2)/4D_h t'} dt'
\end{aligned} \tag{6.27}$$

While the holes arriving at the detector back plane recombine with electrons supplied from the cathode electrode and do not contribute to the accumulating charge signal at the pixel electrode, the electrons arriving at the pixel side naturally increase the surface charge at the input capacitor. The amount of electron charge per unit area arriving at time t at the pixel point (x_p, y_p) during a time dt is equal to

$$d\sigma_{e,arrived}(x_p, y_p, t) = \rho_{e,moving}(x_p, y_p, 0, t)v_e dt \tag{6.28}$$

Thus the contribution of the arrived electrons to the surface charge at the pixel is

$$\begin{aligned}\sigma_{e,arrived}(x_p, y_p, t) &= \int_0^t \rho_{e,moving}(x_p, y_p, 0, t')v_e dt' \\ &= \int_0^t \frac{eN_0}{(4\pi D_e t')^{3/2}} v_e e^{-t'/\tau_e} e^{-((x_p - x_0)^2 + (y_p - y_0)^2 + (-z_0 + v_e t')^2)/4D_e t'} dt'\end{aligned} \tag{6.29}$$

Applying equations 6.27 to equation 6.16 and adding equation 6.29 we then get the expression for the induced surface charge as

$$\begin{aligned}\sigma(x_p, y_p, t) &= -\sigma_{e,arrived}(x_p, y_p, t) \\ &\quad -\frac{1}{4\pi}\int_{-\infty}^{\infty}\int_{-\infty}^{\infty}\int_0^L (\rho_{e,moving} + \rho_{e,trapped} + \rho_{h,moving} + \rho_{h,trapped}) \times \sum_{k=-\infty}^{\infty} G_k \, dxdydz\end{aligned} \tag{6.30}$$

The total induced charge at the pixel at time t can be calculated by inserting equation 6.30 into equation 6.17:

$$Q_{signal}(t) = \int_{-a/2}^{a/2}\int_{-b/2}^{b/2} \sigma(x_p, y_p, t) dx_p dy_p \tag{6.31}$$

where a and b are the pixel x and y dimensions, respectively.

Assuming ohmic metal contacts for both the cathode and anode electrodes the detector leakage current/pixel is given as

$$I_{leak} = \frac{V}{\rho L} A_{pix} \tag{6.32}$$

where V is the bias voltage, ρ the bulk resistivity of the detector material, L the detector thickness and A_{pix} the pixel area. The noise generated by the leakage current can be included in the calculation of the total signal charge by adding to equation 6.31 a noise charge randomly selected from a gaussian distribution with a standard deviation

$$q_{noise} = \sqrt{2 I_{leak} t_{\text{int}} e} \tag{6.33}$$

where t_{int} is the signal integration time and e the elementary charge.

Since the full numerical solution of equation 6.31 would require fairly high computational power some approximations are suggested.

Fisrtly, since we are primarily interested in the total accumulated charge signal at a signal integration time long enough for all the moving electrons to reach the pixel electrode we may exclude the moving electron distribution from the calculations.

Secondly, since the holes move away from the pixel electrode one may consider using a point charge approximation for the moving holes and a line charge approximation for the trapped holes instead of the real gaussian distribution:

$$\begin{aligned} \rho_{h,moving,po\,\text{int}} &= eN_0 e^{-t/\tau_h} \delta(x - x_0)\delta(y - y_0)\delta(z - z_0 - v_h t) \\ \rho_{h,trapped,line} &= \int_0^t eN_0 \frac{1}{\tau_h} e^{-t'/\tau_h} \delta(x - x_0)\delta(y - y_0)\delta(z - z_0 - v_h t)dt' \end{aligned} \tag{6.34}$$

To verify the validity of equations 6.34 we may study the ratio of the full width half maximum (FWHM) of the moving hole charge cloud to the distance from the pixel at different interaction points z_0. The FWHM of the gaussian charge distribution of equation 6.24 is

$$FWHM = 4\sqrt{Dt \ln 2} \tag{6.35}$$

Applying equation 6.19 for the diffusion constant and using $t = (z - z_0)/v_h = (z - z_0)/\mu_h E$ equation 6.35 becomes

$$FWHM = 4\sqrt{\frac{kT}{eE}(z - z_0)\ln 2} \tag{6.36}$$

Plotting FWHM/z according to equation 6.36 reveals that even at an interaction close to the pixel the charge spread is never more than 6 % of the distance from the pixel. Simulation tests show an error in the calculated pixel surface charge contribution of the moving holes of less than 1 % if a point charge is used instead of the real diffused hole charge distribution. Similarly the real distribution of trapped holes may be substituted by a line distribution.

Thirdly we consider the distribution of the trapped electrons. Since the electrons move towards the pixel the line charge approximation is hard to justify from the lateral distribution FWHM to distance from pixel relation. However, one may hope that even if the surface charge distribution induced by the trapped electrons is affected by the diffusion, the total charge integrated over the whole pixel is not significantly different if a line distribution is used for the trapped electrons instead of the real gaussian distribution. The true three dimensional distribution of the trapped electrons is rather heavy to compute and, therefore, a two dimensional approximation neglecting the vertical charge spread and limiting the diffusion to the x and y directions was used in comparison with the line approximation. The error introduced by the line approximation was observed to be very small and hence the line charge approximation was accepted also for the trapped elecrons.

Finally, the sum in equation 6.30 may be investigated to find out how many terms need to be included in the calculations to ensure adequate accuracy. Clearly the terms $|k| > 0$ become more significant when the charge is far away from the pixel (see figure 6.8), i.e., when $z >> 0$. On the other hand, when z approaches L the contribution of the charge located at z is minimal due to the small pixel effect. The conclusion which was verified by simulation tests is that adequate accuracy is maintained even if terms with $|k| > 1$ are excluded.

We may conclude the consideration of approximations by writing the equation for the approximate surface charge which was used in the simulations for integration times large enough to collect all the moving electrons surviving trapping:

$$\sigma(x_p, y_p, t) = -\sigma_{e,arrived}(x_p, y_p, t) - \frac{1}{4\pi}\int_{-\infty}^{\infty}\int_{-\infty}^{\infty}\int_{0}^{L}(\rho_{e,trapped,line} + \rho_{h,moving,point} + \rho_{h,trapped,line}) \times \sum_{k=-1}^{1} G_k \, dxdydz \tag{6.37}$$

Thus the effect of the carrier diffusion is included only in the calculation of the electrons arrived at the pixel input.

The integrals in equation 6.37 were calculated numerically using step sizes which were a compromise between accuracy and speed. The charge distributions were integrated with a step size of 10 μm. For the moving and trapped carriers the pixel electrode was divided into 625 squares (step size = pixel size/25) and the total induced signal charge was calculated as the sum of the induced charge in these squares. The gaussian distribution of the arrived electrons was integrated over ± 4 standard deviations (σ) with a step size equal to 8σ/50.

The energy spectra were simulated by calculating the total induced charge of 10,000 gamma rays with randomly chosen interaction points (x_0, y_0, z_0). The distribution of the interaction points was uniform in the x and y directions between ± pixel dimension/2 and exponential in the z direction according to the photo electric absorption coefficient for 140 keV gamma rays (see table 1). To avoid calculation errors from gamma absorption close to the pixel electrode the z interaction points were limited to 10 μm < z_0 < L.

The material parameters generally used in the simulations were adopted from [64] and are presented in table 6.1. A signal integration time of 500 ns was used to simulate the case of fast counting in high intensity gamma imaging. For comparison with experimental data of other works parameters given in those publications were used.

The simulation program was coded in LabVIEW™.

Parameter	CdTe	CdZnTe
Resistivity (ρ)	10^9 Ωcm	10^{11} Ωcm
e-h pair creation energy ($E_{e\text{-}h}$)	4.43 eV	5.00 eV
Electron mobility (μ_e)	1100 cm^2/Vs	1350 cm^2/Vs
Electron life time (τ_e)	3.0 μs	1.0 μs
Hole mobility (μ_h)	100 cm^2/Vs	120 cm^2/Vs
Hole life time (τ_h)	2.0 μs	0.05 μs
Photo electric absorption coefficient at 140 keV	3.441 cm^{-1}	3.210 cm^{-1}
Signal integration time (t_{int})	500 ns	500 ns
Gamma energy (E_γ)	140 keV	140 keV

Table 6.1. Simulation parameters.

6.4.2 Simulation results

Figure 6.10 shows two simulation examples of the surface charge distribution σ on the pixel electrode. Figure 6.10a illustrates the contribution of the trapped holes and trapped electrons for a

gamma interaction close to the pixel electrode and figure 6b the distribution of the collected but diffused electrons when the gamma ray was absorbed far away from the pixel.

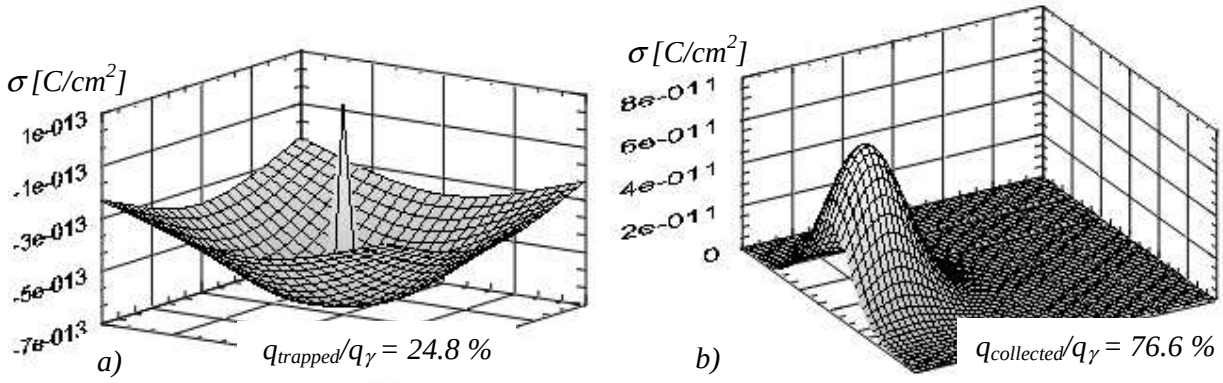


Figure 6.10. Simulated surface charge distributions on one pixel electrode of a CdZnTe detector at t_{int} = 2000 μs after a gamma interaction (L = 2 mm, V_{bias} = 200 V). Material parameters used are given in table 6.1. a) Contribution of trapped holes and trapped electrons ($q_{trapped}/q_\gamma$) when z_0 = 0.28 mm, x_0 = y_0 = 0 and pixel size = 500 μm, b) Contribution of collected electrons ($q_{collected}/q_\gamma$) when z_0 = 1.7 mm, x_0 = 0, y_0 = 100 μm and pixel size = 250 μm.

The reliability of the model was tested by comparing simulated spectra with experimental spectra presented in [98]. Figure 6.11 shows simulated spectra with CdZnTe parameters and pixel sizes adapted from [98, page 658, fig. 15]. Remembering that the model in this work does not take into account the compton scattered rays and that only gamma interactions within the pixel area are considered it may be concluded that the simulation results agree well with this experimental data. Despite the slight difference between the experimental and simulated data of the spectra of the 1000 μm and 250 μm pixels the simulated dependency of the spectral quality on the pixel size is in excellent agreement with the experimental result.

To determine the performance of CdTe and CdZnTe pixel detectors in high intensity gamma imaging the photo peak efficiency as defined in equation 6.15 was calculated from simulated energy spectra as the photo electric absorption efficiency multiplied by the percentage of hits above a threshold energy equal to 95 % of the 140 keV photo peak energy. Figure 6.12 shows examples of simulated energy spectra of both CdTe and CdZnTe detectors (parameters from table 6.1) for two pixel sizes. Due to the shorter hole life time the low energy tailing of the spectral peak is somewhat worse for the CdZnTe detector. On the other hand, the lower resistivity of the CdTe detector results in a higher leakage current and a wider photo peak compared to the CdZnTe detector. The shift of the photopeak to the left for the CdZnTe detectors is due to the lower electron life time. Both detectors suffer from significant lateral charge signal diffusion at the smaller pixel size.

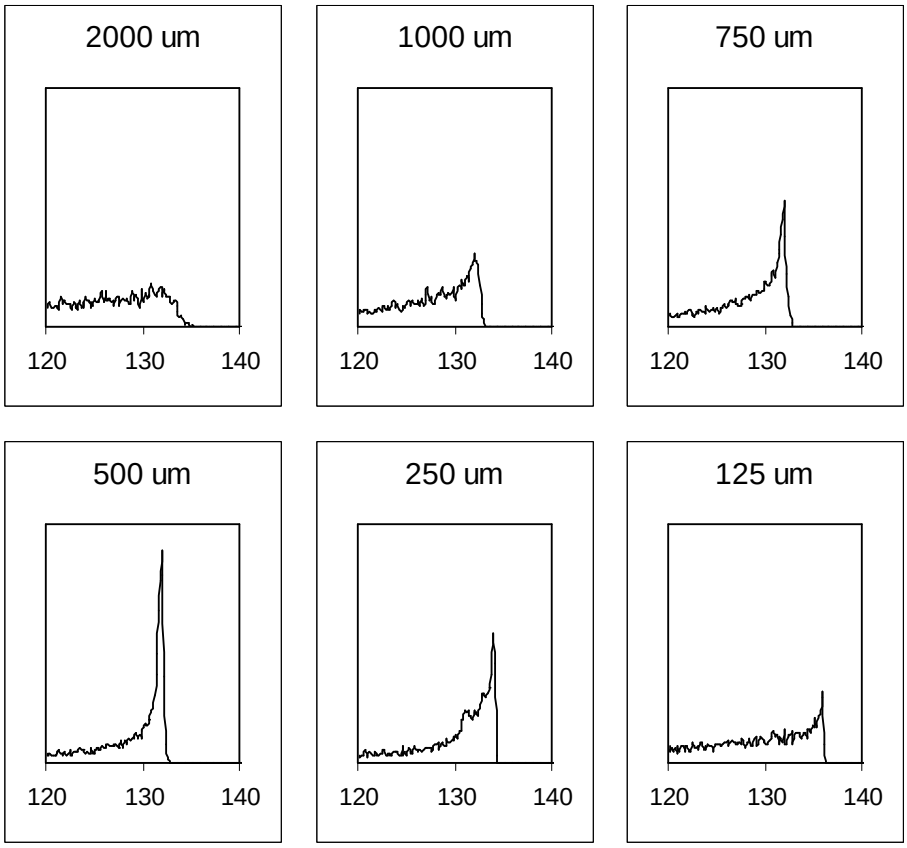


Figure 6.11. Simulated energy spectra for different pixel sizes of a CdZnTe detector. The spectra have been normalised to contain an equal number of counts in the shown window. Material parameters were adapted from [98] as τ_e = 1.48 μs, τ_h = 0.17 μs, L = 0.15 cm, V_{bias} = 150 V, t_{int} = 2000 μs. Other parameters as in table 6.1.

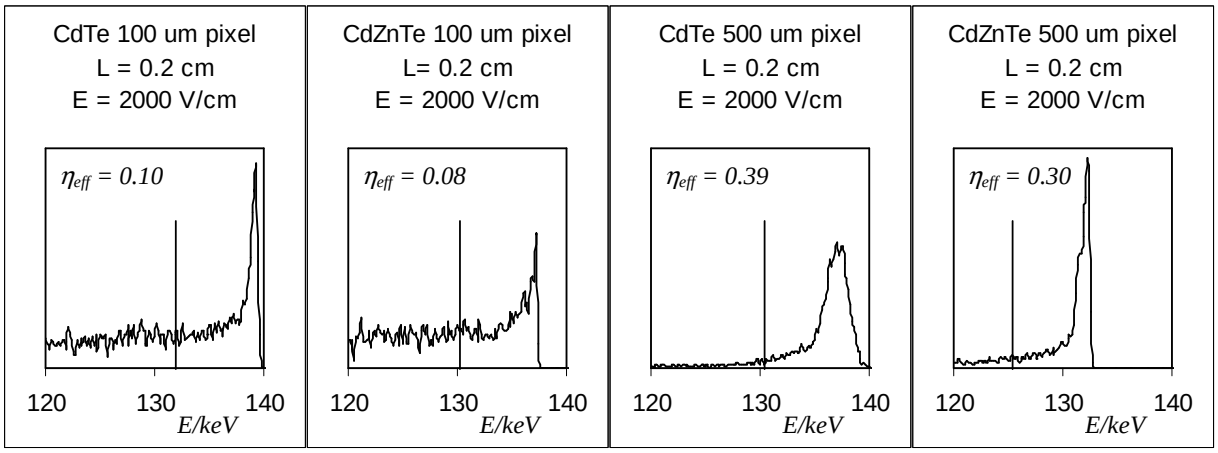


Figure 6.12. Examples of simulated energy spectra. The 95 % threshold is shown as a vertical line. The photo peak efficiency η_{eff} is defined as the percentage of counts above the threshold multiplied by the photo electric absorption efficiency.

Figure 6.13 presents the simulated η_{eff} as a function of the pixel size at various values of the detector thickness for both CdTe and CdZnTe. The η_{eff} curves rises with increasing pixel size to a maximum value at an optimum pixel size after which the small pixel effect dominates over charge diffusion. The small pixel effect is stronger for CdZnTe due to the shorter hole life time. Thick CdZnTe detectors also suffer from electron trapping which (in opposite to hole trapping) affects small pixels more than large ones. This results in higher η_{eff} for thinner CdZnTe detectors at small pixel sizes. The optimum CdZnTe detector thickness for 500 μm pixels, e.g., is around 3 mm as can be seen in figure 6.14. For CdTe, thicker detectors yield higher η_{eff} above pixel sizes of 250 μm but increasing the thickness, e.g., from 4 mm to 5 mm for 500 μm pixels gives only a minor improvement in the CdTe η_{eff}. The η_{eff} values of CdTe are generally better than those of CdZnTe partly because of the slightly higher photo electric absorption coefficient but mostly because of the stronger effect of signal charge trapping in CdZnTe. η_{eff} falls rapidly at pixel sizes below 250 μm.

The photo peak efficiency can be somewhat improved by increasing the electric field strength as shown in figure 6.15.

As can be seen in figure 6.16 the energy resolution is generally better with CdZnTe detectors due to the higher resistivity and lower leakage current.

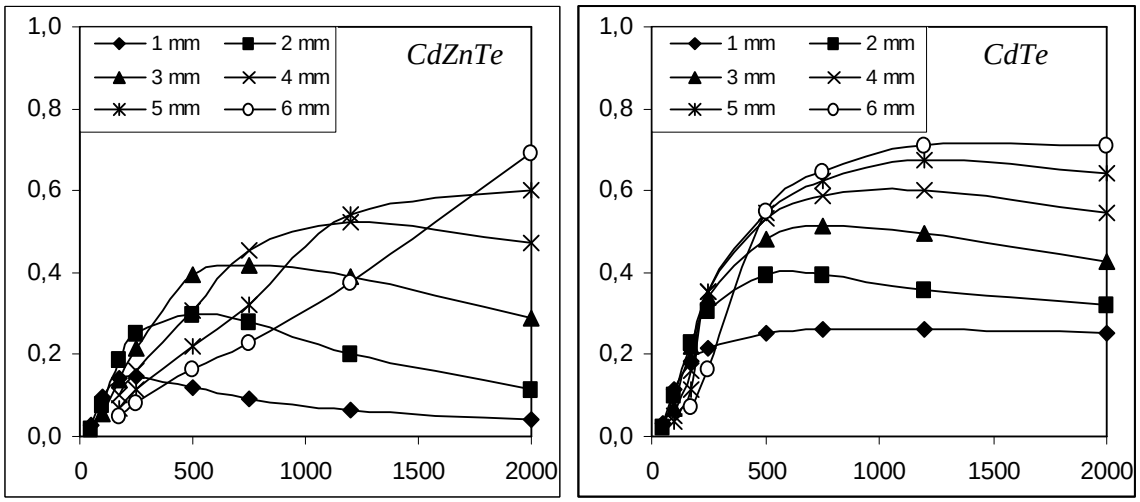


Figure 6.13. The simulated photo peak efficiency η_{eff} as a function of the pixel size for various detector thicknesses L (see legend) for a) CdZnTe and b) CdTe.

In conclusion it can be said that the photo peak efficiency is adequate for gamma imaging for pixel sizes down to at least 500 μm which means that the spatial resolution of conventional gamma cameras will be significantly improved when the scintillator coupled PM tubes are substituted with

monolithic CdTe detectors. On the other hand because of the signal charge diffusion effect it is quite obvious that some fancy ideas of designing photo counting CdTe detectors with pixel sizes of 50 μm for high intensity X-ray imaging are not realistic [121,124]. The simulation results also indicate that optimum η_{eff} is not always achieved with maximum detector thickness. Since the price of CdTe/CdZnTe is proportional to the crystal volume this result should be of interest to commercial manufacturers of gamma cameras.

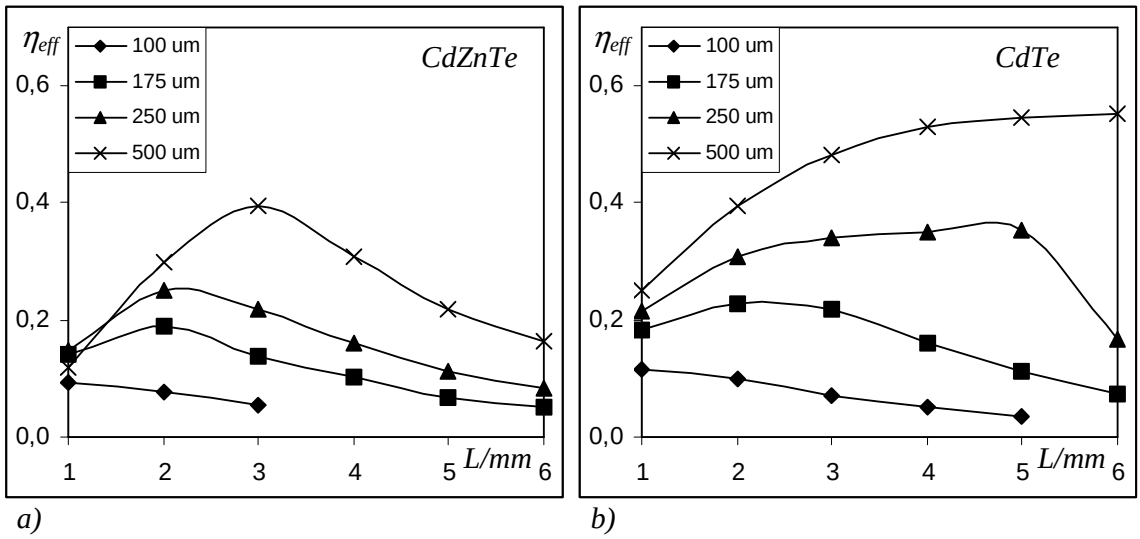


Figure 6.14. The simulated photo peak efficiency η_{eff} as a function of detector thickness L for various pixel sizes (see legend) for a) CdZnTe and b) CdTe.

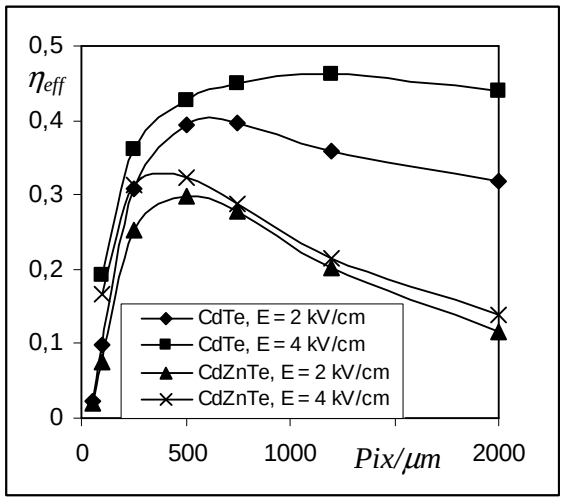


Figure 6.15. The simulated photo peak efficiency η_{eff} as a function of the pixel size for two different electric field strengths for CdTe and CdZnTe (L = 2 mm).

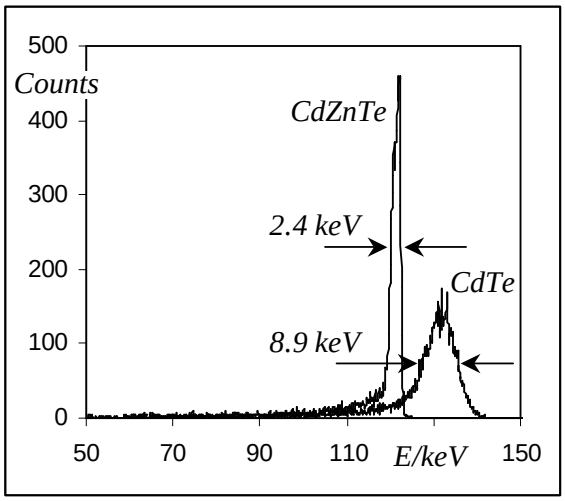


Figure 6.16. Simulated energy spectra for CdTe and CdZnTe (L = 2 mm, pixel size = 2000 μm, E = kV/cm).

Energy spectra were eventually simulated with appropriate parameters to model the CdTe detectors used in the gamma camera developed at Oy Ajat Ltd. as described in [Publication VIII]. These simulations agree well with experimental data proving the value of the model in the estimation of the photo peak efficiency of photon counting pixel detectors (see especially figure 3 of [Publication VIII]).

Other issues related to the perfromance of the Ajat gamma camera are discussed in [Publication VIII].

7. Radiation hardness issues

When radiation detectors are used to measure the intensity and energy of ionizing radiation they are naturally also exposed to the harmful effects of radiation on matter. This may lead to damage in the detectors and to the associated readout electronics.

Ionizing radiation effects in CMOS circuits have been widely investigated and the radiation damage mechanisms are well known [101]. Several studies on radiation induced damage in high resistivity silicon detectors have been carried out and the effects in Si detectors are equally well understood [27,102-105]. Less work exist on the radiation tolerance of CdTe and CdZnTe detectors but experimental results on the effect of ^{60}Co gamma and neutron radiation [106,107] and proton radiation [110] have been published

Since this work deals with detectors for X- and low energy gamma radiation applications the effects of particle radiation is not of interest. Unlike neutron, proton and other particle radiation X-rays do not change the bulk properties of semiconductor crystals and hence only surface effects in the oxide layers of the detectors and CMOS chips are considered. High energy gammas may cause bulk damage through Compton electrons but gamma rays of a maximum energy of 140 keV (used in medical gamma imaging) do not affect the crystal structure of solids [108].

7.1 Dose determination

Surface damage in oxide layers of semiconductor components depends on the total absorbed dose rather than on the energy of the radiation. Because of annealing effects the dose rate may also affect the induced damage.

The dose in a radiation damage experiment is typically measured with an air filled ionization chamber. If E_γ is the energy of the electromagnetic radiation, I the intensity, A and d_{air} the area and thickness of the chamber, respectively, ρ_{air} the air density and μ_{air} the energy absorption coefficient of air in cm^2/g then the absorbed dose/time in the chamber is

$$Dose_{air} = \frac{AI(1-e^{-\mu_{air}(E)\rho_{air}d_{air}})}{Ad_{air}\rho_{air}}E_\gamma = \frac{I(1-e^{-\mu_{air}(E)\rho_{air}d_{air}})}{d_{air}\rho_{air}}E_\gamma \qquad (7.1)$$

Similarly, the absorbed dose/time in an oxide layer is

$$Dose_{oxide} = \frac{I(1-e^{-\mu_{oxide}(E)\rho_{oxide}d_{oxide}})}{d_{oxide}\rho_{oxide}} E_{\gamma} \qquad (7.2)$$

Then

$$\frac{Dose_{air}}{Dose_{oxide}} = \frac{d_{oxide}\rho_{oxide}(1-e^{-\mu_{air}(E)\rho_{air}d_{air}})}{d_{air}\rho_{air}(1-e^{-\mu_{oxide}(E)\rho_{oxide}d_{oxide}})} \qquad (7.3)$$

If the absorbers are thin we may use the approximation $e^x \approx 1 + x$ and write

$$\frac{Dose_{air}}{Dose_{oxide}} \approx \frac{d_{oxide}\rho_{oxide}\mu_{air}(E)\rho_{air}d_{air}}{d_{air}\rho_{air}\mu_{oxide}(E)\rho_{oxide}d_{oxide}} = \frac{\mu_{air}(E)}{\mu_{oxide}(E)} \qquad (7.4)$$

An absorbing layer can be considered thin if the absorbtion is uniform throughout the layer. This may not be true for low energies and, therefore, for an accurate dose determination low energies should be filtered out if polyenergetic beams are used in the experiments. Since the absorbtion coefficients depend on the radiation energy the actual dose absorbed in the oxide layer under consideration depends not only on the dose measured with the ionization chamber but also on the radiation energy. For a polyenergetic beam N(E) equation 7.4 becomes

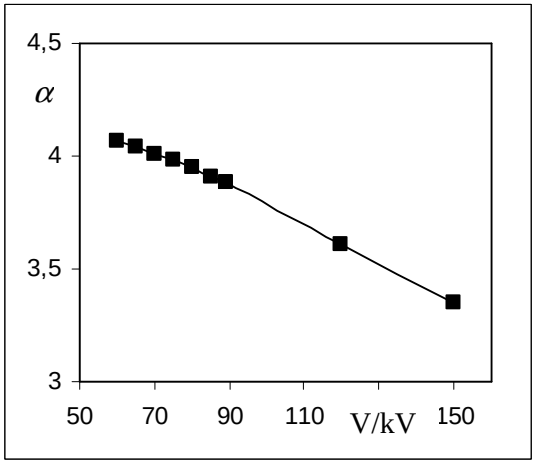


Figure 7.1. The ratio of the absorbed dose in a SiO_2 layer to the dose measured with an ionization chamber as a function of the X-ray spectrum generator voltage.

$$\frac{Dose_{air}}{Dose_{oxide}} \approx \frac{\int N(E)\mu_{air}(E)EdE}{\int N(E)\mu_{oxide}(E)EdE} \Rightarrow Dose_{oxide} = \frac{\int N(E)\mu_{oxide}(E)EdE}{\int N(E)\mu_{air}(E)EdE} Dose_{air} = \alpha Dose_{air} \qquad (7.5)$$

The coefficient α depends on the spectrum used and is plotted in figure 7.1 as a function of the X-ray generator tube voltage for X-ray spectra filtered with 1 mm aluminium. In [Publication VI] a 60 kV beam with 1 mm Al filtration is used in the radiation hardness tests and the dose is given as krad

in air. The dose conversion coefficient α for this beam is 4.07 and may be used to convert the given krad(air) doses to krad(SiO_2).

7.2 CMOS electronics

Ionizing radiation creates Si-SiO_2 interface states and induces positive charge in the gate and field oxide layers of CMOS circuits which in turn may cause flat band shifts in MOS structures and inversion layers at the Si surface and consequent surface leakage currents [101].

Since integrated circuits are processed on p type silicon inversion first occurs as an electron layer underneath the field oxide layer covering the p bulk. This electron layer may form a conducting path between n^+ implantations such as transistor sources and drains. The radiation hardness can be improved (rad hard CMOS processing) by substituting NMOS with PMOS transistors (inversion is not formed by positive oxide charge in the n well of PMOS transistors), by using closed gate designs which prevent leakage paths or by p^+ guard structures which cut electron inversion layers. Serious defects which deteriorate the circuit performance are usually not observed even in non rad hard conventional CMOS circuits before a dose of several tens of krad [115]. In this work, however, it was observed that even a very low dose of less than 1 krad can be fatal for a charge integrating preamplifier if the input gate design is incorrect. The problem of the radiation hardness of the developed intra oral X-ray imaging sensor and the solution to this problem is presented in [Publication VI].

Some radiation hardness problems in the CMOS pixel cirucits developed for the CdTe imagers during this work were also observed [109]. These are currently under investigation.

7.3 Silicon detectors

Positive oxide charge creates electron layers at the surface of the n type crystal of Si radiation detectors. Electron accumulation between p^+ implantations is not a problem but if n^+ sructures are used such as in double sided strip detectors the reduced surface resistance may cause problems [104,105].

The radiation induced increase in the Si-SiO_2 interface state density increases the surface generation current which results in higher detector dark current [111]. In this work increased dark currents were observed for the first pixel detectors designed for the intra oral sensor. These detectors were manufactured at Sintef, Norway [112]. Later detectors processed at Colibrys, Switzerland [113], were observed to show no increase in the dark current at dental doses

[Publication VI]. The different radiation tolerance of the detectors supplied by Sintef and Colibrys is related to the secrets of the oxidation process.

7.4 CdTe and CdZnTe detectors

Conventionally CdTe and CdZnTe detectors are manufactured by simply depositing metal contacts onto the semiconductor surface. If such detectors are used in X- and low energy gamma ray applications radiation damage is not an issue. However, the pixel detector manufacturing process described in section 5.2 includes AlN passivation on the CdTe/CdZnTe surface. It is possible that radiation induced positive charge accumulates in this passivation layer or that interface states are created at the AlN-CdTe interface. The consequences could be reduced interpixel resistance and higher leakage current. This is an interesting issue which remains to be studied.

One important application for the CdTe imager described in chapter 5 is on line non-destructive testing of printed circuit boards. In this application the beam voltage is typically 160 kV [114]. Due to continuous on line use the accumulated doses are high and radiation induced damage will limit the sensor life time. The most sensitive component is the CMOS pixel circuit. The highly absorbing CdTe pixel detector serves to protect the CMOS readout circuit and the sensor radiation tolerance can be improved by increasing the CdTe detector thickness. Figure 7.2 shows how the energy spectrum produced with a tube voltage of 150 kV and a current of 100 μA and filtered with 0.5 mm Al changes when passing through CdTe detectors of different thickness. The annual dose (assuming 24 h 365 d continuous use and 25 cm source to sensor distance) absorbed in the CMOS circuit is given in krad(SiO_2) for the three detector thicknesses.

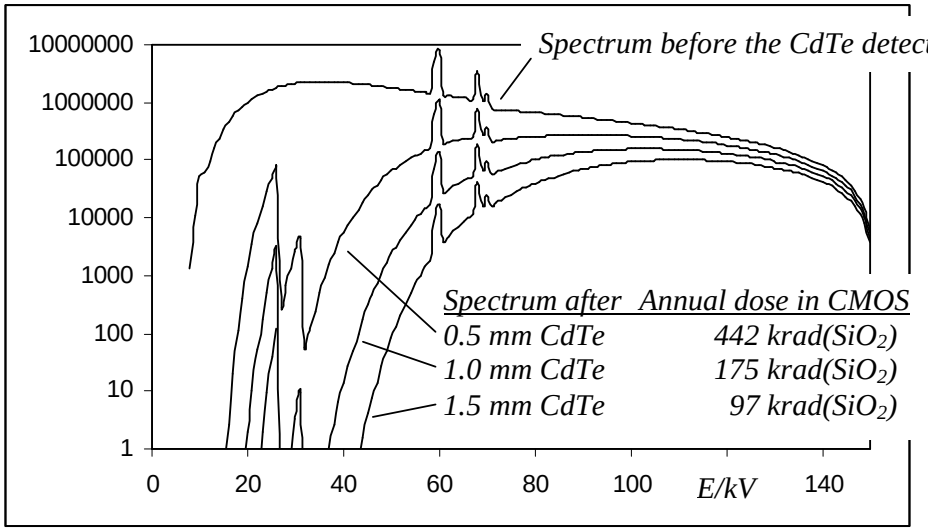


Figure 7.2. The calculated effect of the CdTe detector thickness on the absorbed dose in the CMOS pixel circuits of a CdTe real time imager.

8. Conclusions

The research and development described in the preceding chapters have shown that directly converting crystalline semiconductor pixel detectors operated in the charge integration mode can be used in X-ray imaging very close to the theoretical performance limits in terms of efficiency and resolution. This means that the frequency dependent DQE is ultimately determined by the pixel size of the detector and the X-ray absorption efficiency of the semiconductor material. Thus crystalline semiconductor detectors bump bonded to CMOS signal readout circuitry are optimal for X-ray imaging and has the potential of subsituting flat panel and optically coupled CCD systems and of being the technology of next generation digital X-ray imagers. However, some manufacturing problems remain, the most serious being the limited sensor area. It is quite evident that no technical solution will be available in the near future to enable truly large continuous imaging areas with crystalline semiconductors and CMOS integrated circuits.

It seems, therefore, that while amorphous semiconductor flat panels will continue to compete with film in conventional large area radiology such as chest X-ray imaging, crystalline semiconductors capable of high resolution imaging will be applied to more specific problems. Any X-ray imaging which allows scanning for image acquisition and requires high resolution and efficiency will most probably in the not too far future be performed with crystalline semiconductors connected to CMOS readout circuits. Perhaps the most important and challenging of such applications is mammography. Since the X-ray energy used in mammogarphy is low even silicon detectors are suitable for digital mammography [116-118]. The final solution to digital mammography for optimum performance could be a scanning CdTe-CMOS pixel sensor.

CdTe photon counting sensors promise significant improvements in nuclear medicine gamma imaging. Simulations presented in this work and recent experimental results [82, Publication VIII] predict an achievable spatial resolution of 1 lp/mm and an energy resolution of 5 – 10 % for CdTe gamma cameras.

While technological problems of CdTe detector manufacturing related to thin film processing and bump bonding are more or less solved the availability of high quality CdTe crystals may turn out to be a bottle neck in commercial applications. At the moment there is apparently only one CdTe material supplier which has reached an acceptable level of crystal quality for imaging applications [62]. But with the medical sector as the driving force it is most likely that the development of CdTe crystal growth will not come to an end and that in the near future the CdTe availability will improve.

References

[1] J. Kemmer, *Fabrication of low noise silicon radiation detectors by the planar process*, NIM 169, 1980.

[2] J. Kemmer, *Improvement of detector fabrication by the planar process*, NIM A 226, 1984.

[3] E. H. M. Heijne et al., *A silicon surface barrier microstrip detector designed for high energy physics*, NIM 178, 1980.

[4] M. Caccia et al., *A Si strip detector with integrated coupling capacitors*, NIM A 260, 1987.

[5] N. Bingefors et al., *The Delphi Microvertex detector*, NIM A 328, 1993.

[6] C. Bozzi et al., *First-year experience with the BaBar silicon vertex tracker*, NIM A 473, 2001.

[7] B. Sanghera et al., *Digital beta autoradiography using silicon microstrip detectors*, NIM A 310, 1991.

[8] M. Overdick et al., *A "Bioscope" system using double-sided silicon strip detectors and self-triggering read-out chips*, NIM A 392, 1997.

[9] A. Czermak et al., *A new 2-dimensional high resolution Si detector for β-and γ-radiography*, NIM A 360, 1995.

[10] F. Arfelli, *Silicon detector for synchrotron radiation digital radiology*, NIM A 353, 1994.

[11] P. Jalas et al., *New results with semiconductor drift chambers for X-ray spectroscopy*, IEEE Trans. Nucl. Sci. Vol. 42, 1994.

[12] J. Kemmer and G. Lutz, *New detector concepts*, NIM A 253, 1987.

[13] H. Soltau et al., *Fabrication, test and performance of very large X-ray CCDs designed for astrophysical applications*, NIM A 439, 2000.

[14] E. H. M. Heijne, *Semiconductor micropattern pixel detectors: a review of the beginnings*, NIM A 465, 2001.

[15] T. Mouthy, *Silicon pixel detector research and development*, NIM A 368, 1995.

[16] K. S. Kump, *Fast imaging of a 41cm aSi flat panel detector for radiographic applications*, Proceedings of SPIE, Physics of Medical Imaging, Vol. 4320, 2001

[17] Watanabe et al., *Development and evaluation of a portable amorphous silicon flat-panel x-ray detector*, SPIE Vol. 4320, 2001.

[18] D. L. Lee et al., *Imaging performance of a direct digital radiographic detector using Selenium and a thin-film-transistor array*, Computer Assisted Radiology, 1996.

[19] M. Yaffe and J. A. Rowlands, *X-ray detectors for digital radiography*, Phys Med. Biol. 42, 1997.

[20] J. M. Henry et al., *Solid state detectors for digital mammography*, SPIE Vol. 2432, 1995.

[21] M. Cuzin et al., *Preliminary characterization of a new hybrid structure with CdTe: X-ray imaging capabilities,* SPIE Vol. 2278, 1994.

[22] E. Samei et al., *DQE of direct and indirect digital radiography systems,* SPIE Vol. 4320, 2001.

[23] E. Bertolucci et al., *X-ray imaging using a pixel GaAs detector,* NIM A 362, 1995.

[24] B. E. Patt, *Development of a mercuric iodide detector array for medical imaging applications,* NIM A 366, 1995.

[25] C. Scheiber, *CdTe and CdZnTe detectors in nuclear medicine,* NIM A 448, 2000.

[26] R. Orava, *The SEFT detector laboratory and its role in Finnish high energy physics*, Research Institute for High Energy Physics (SEFT), University of Helsinki, Finland, 1996.

[27] M. Laakso, *Radiation detection techniques for high energy physics and industrial applications,* Report series HU-SEFT RD 1993-01, University of Helsinki, Finland, 1993.

[28] P. Weilhammer, *Overview: silicon vertex detectors and trackers*, NIM A 453, 2000.

[29] H.-G. Moser, *Experience with the ALEPH silicon vertex detector,* NIM A 310, 1991.

[30] G. Bencze et al., *Silicon tracker for LHC*, Nuclear Physics B (Proc. Suppl.) 32, 1993.

[31] S. I. Parker et al., *3D – A proposed new architecture for solid-state radiation detectors*, NIM A 395, 1997.

[32] http://www.brunel.ac.uk/research/rose/3D/3ddetectors.html.

[33] G. F. Knoll, *Radiation detection and measurement*, Third edition, p. 115, John Wiley & Sons, 2000.

[34] Z. Jing et al., *Design of a high resolution digital imaging system for mammography*, Presented at the 36th AAPM annual meeting, Anaheim, CA, USA, 1994.

[35] M. Gambaccini et al., *MTF evaluation of a phosphor-coated CCD for X-ray imaging,* Phys. Med. Biol. 41, p. 2799, 1996.

[36] J. P. Moy, *Image quality of scintillator based X-ray electronic imagers*, SPIE Vol. 3336, 1998.

[37] E. Samei et al., *DQE of direct and indirect digital radiographic systems*, Proc. SPIE 4320: 189-197, 2001.

[38] G. F. Knoll, *Radiation detection and measurement*, Third edition, p. 329, John Wiley & Sons, 2000.

[39] R. M. Harrison, *Digital Radiography,* Phys. Med. Biol., No. 7, 1988.

[40] H. Liu et al., *Lesion detectability conciderations for an optically-coupled CCD X-ray imaging system*, IEEE Trans. Nucl. Sci. Vol. 41, No. 4, 1994.

[41] J. Watt, *Photon counting vs. charge integration – experimental studies with a GaAs hybrid pixel detector*, Presented at the IWoRID workshop in Freiburg, Germany, July 2000.

[42] M. Sandborg and G. A. Carlsson, *Influence of X-ray energy spectrum, contrasting detail and detector on the signal-to-noise ratio (SNR) and detective quantum efficiency (DQE) in projection radiography*, Phys. Med. Biol. 37, p. 1245-1263, 1992.

[43] F. Pedersen and M. Sandborg, *Using a hybrid pixel detector for dynamic radiography*, Presented at the IEEE Nuclear science symposium and Medical imaging conference, Anaheim, CA, USA, 1996.

[44] C. Schwarz et al., *Measurements with Si and GaAs pixel detectors bonded to photon counting readout chips*, NIM A 466, 2001.

[45] H. Roehrig et al., *Application of hybrid detector technology for digital mammography*, SPIE Vol. 2519, 1995.

[46] A. Martinez-Davalos et al., *Evaluation of a new low-dose digital X-ray system*, Phys. Med. Biol. 38, p. 1419-1432, 1993.

[47] A. Jalink et al., *CCD mosaic technique for large-field digital mammography*, IEEE Transactions om medical imaging, Vol. 15, No. 3, 1996.

[48] K. Spartiotis et al., *A novel semiconductor pixel device and system*, Presented at the IEEE Medical Imaging Conference, LA, USA, 1996.

[49] Imix Oy, Hermia Science Park, Tampere, Finland.

[50] B. S. Avset and L. Evensen, *The effect of metal field plates on multiguard structures with floating p^+ guard rings*, NIM A 377, 1996.

[51] Detection Technology Inc., Ii, Finland, www.deetee.com.

[52] R. Brenner et al., *Measurement of the spatial resolution of double-sided double-metal AC-coupled silicon microstrip detectors*, NIM A 326, 1993.

[53] G. F. Knoll, *Radiation detection and measurement*, Third edition, p. 355, John Wiley & Sons, 2000.

[54] www.atmel.com

[55] L. Verger et al., *Characterization of CdTe and CdZnTe detectors for gamma-ray imaging applications*, NIM A 458, 2001.

[56] Amptek, Inc., www.amptek.com

[57] A. Shor et al., *Spectroscopy with pixelated CdZnTe gamma detectors – experiment versus theory*, NIM A 458, 2001.

[58] T. H. Prettyman et al., *Characterization of a large-volume multi-element CdZnTe detector*, SPIE 4141, 2000.

[59] Y. Nemirovsky et al., *Recent progress in n-type CdZnTe arrays for gamma-ray spectroscopy*, NIM A 458, 2001.

[60] K. B. Parnham et al., *Development of a CdZnTe-based Small Field of View Gamma Camera*, SPIE 4508, 2001.

[61] H. B. Barber et al., *Semiconductor pixel detectors for gamma-ray imaging in nuclear medicine*, NIM A 395, 1997.

[62] www.acrorad.com

[63] G. F. Knoll, *Radiation detection and measurement*, Third edition, p. 486, John Wiley & Sons, 2000.

[64] www2.ocn.ne.jp/~raytech/raytech_032.htm

[65] Y. Eisen et al., *CdTe and CdZnTe gamma ray detectors for medical and industrial imaging systems*, NIM A 428, 1999.

[66] G. F. Knoll, *Radiation detection and measurement*, Third edition, p. 480, John Wiley & Sons, 2000.

[67] T. Takahashi et al., *High-resolution Schottky CdTe diode for hard X-ray and gamma-ray astronomy*, NIM A 436, 1999.

[68] M. Funaki, *Growth and characterization of CdTe single crystals for radiation detectors*, NIM A 436, 1999.

[69] P. Capper, editor, *Properties of Narrow Gap Cadmium-based Compounds*, Emis Datareview Series No.10, p. 579, 1994.

[70] C. Matsumoto et al., *Performance of a new Schottky CdTe detector for hard X-ray spectroscopy*, IEEE Transactions on Nuclear Science, Vol. 45, 1998.

[71] T. E. Schlesinger et al., *Cadmium zinc telluride and its use as a nuclear radiation detection material*, Materials Science and engineering, 32, 2001.

[72] D. Vartsky et al., *Radiation induced polarization in CdTe detectors*, NIM A 263, 1988.

[73] A. Kh. Khusainov, *High performance p–i–n CdTe and CdZnTe detectors*, NIM A 428, 1999.

[74] M. Niraula et al., *Stability issues of high-energy resolution diode type CdTe nuclear radiation detectors in a long-term operation*, NIM A 491, 2002.

[75] K.-L. Giboni and E. Aprile, *Evaluation of CdTe detectors with Schottky contacts for imaging applications*, NIM A 416, 1998.

[76] P. N. Luke et al., *Coplanar-grid CdZnTe detector with three-dimensional position sensitivity*, NIM A 439, 2000.

[77] J. M. Cardoso et al., *CdZnTe spectra improvement through digital pulse amplitude correction using the linear sliding method*, NIM A 505, 2003.

[78] R. Orava et al., U.S. Patent 6,046,068, April 2000.

[79] R. Orava et al., U.S. Patent 6,215,123, April 2001.

[80] K. Spartiotis and H. Heikkinen, U.S. Patent 6,410,922, June 2002.

[81] K. Spartiotis and J. Salonen, U.S. Patent 5,952,646, September 1999.

[82] Oy Ajat Ltd., www.ajat.fi

[83] B. Mikulec et al., *Characterisation of a single photon counting pixel system for imaging of low-contrast objects*, NIM A 458, 2001.

[84] P. Fischer et al., *A counting CdTe pixel detector for hard X-ray and γ-ray imaging*, IEEE Transactions on Nuclear Science, Vol. 48, Issue 6, 2001.

[85] M. Eräluoto, Oy Simage Ltd.

[86] T. Pantsar, Oy Ajat Ltd.

[87] U. Welander, *A mathematical model of narrow beam rotation methods*, Acta Radiologica, Vol. 15, 1974.

[88] Planmeca Oy, www.planmeca.com

[89] J. T. Bushberg et al., *The Essential Physics of Medical Imaging*, Lippincott Williams & Wilkins Publishers, 2nd edition , 2001.

[90] G. F. Knoll, *Radiation detection and measurement*, Third edition, p. 348, John Wiley & Sons, 2000.

[91] T. O. Tümay et al., *High-resolution pixel detectors for second generation digital mammography*, NIM A 497, 2003.

[92] C. Scheiber and G. C. Giakos, *Medical applications of CdTe and CdZnTe detectors*, NIM A 458, 2001.

[93] L. del Risco Norrlid et al., *Calculation of the modulation transfer function for the X-ray imaging detector DIXI using Monte Carlo simulation data*, NIM A 466, 2001.

[94] H. Fujita et al., *A Simple Method for Determining the Modulation Transfer Function in Digital Radioraphy*, IEEE Transactions on medical imaging, Vol.11, No.1, March 1992.

[95] K. Egiazarian, *Signal Processing Laboratory*, Tampere University of Technology.

[96] The mouse was killed accidentally in a mouse trap in Monninkylä Mouse House, Askola, Finland, before it was used in the experiments ☺.

[97] H. H. Barrett et al., *Charge Transport in Arrays of Semiconductor Gamma-Ray Detectors*, Physical Review Letters, Vol. 75, No. 1, 1995.

[98] J.D.Eskin et al., *Signals induced in semiconductor gamma-ray imaging detectors*, J. of Applied Physics, Vol. 85, No. 2, 1999.

[99] S. M. Sze, *Physics of Semiconductor Devices*, p. 50 – 55, John Wiley & Sons, 1981.

[100] E. Gatti et al., *Dynamics of electrons in drift detectors*, NIM A 253, 1987.

[101] T. P. Ma and P. V. Dressendorf (Editors), *Ionizing Radiation Effects in MOS Devices and circuits*, John Wiley & Sons, 1989.

[102] V. A. J. van Lint, *The physics of radiation damage in particle detectors*, NIM A 253, 1987.

[103] M. Nakamura et al., *Radiation damage tests of silicon multistrip detectors*, NIM A 270, 1988.

[104] M. Laakso et al., *Radiation Damage Measurements on Double-Sides Silicon Strip detectors*, Proceedings of the Symposium on Detector Research an Development for the Superconducting Super Collider, Texas, USA, 1990.

[105] T. Schulman, *Radiation Damage in Double-Sided Silicon Strip Detectors*, Report Series HU-SEFT-1991-07, University of Helsinki, Finland, 1991.

[106] A. Cavallini et al., *Electronic properties of traps induced by γ-irradiation in CdTe and CdZnTe detectors*, NIM A 448, 2000.

[107] A. Cavallini et al., *Irradiation-induced defects in CdTe and CdZnTe detectors*, NIM A 458, 2001.

[108] G. F. Knoll, *Radiation detection and measurement*, Third edition, p. 387, John Wiley & Sons, 2000.

[109] F. Garcia, iXimaging plc.

[110] Y. Eisen et al., *Radiation damage of Schottky CdTe detectors irradiated by 200 MeV protons*, NIM A 491, 2002.

[111] C. Becker et al., *Gate-controlled diodes for characterization of the Si–SiO_2 interface with respect to surface effects of silicon detectors*, NIM A 444, 2000.

[112] www.sintef.no

[113] www.colibrys.com

[114] M. Shipley, Agilent Technologies.

[115] T. Clifford, *X-ray Inspection...Easy Does It*, EP&P, February 2002.

[116] M. Danielsson, Mamea Imaging AB, www.mamea.se, Sweden.

[117] Sectra AB, www.sectra.se, Sweden.

[118] B. Hemdal et al., *Mammography – recent technical developments and their clinical potential*, SSI Rapport 2002:08, Swedish Radiation Protection Authority, May 2002, www.ssi.se/ssi_rapporter/pdf/ssi_rapp_2002_08.pdf

[119] K. Puhakka, Oy Ajat Ltd.

[120] T. Pantsar and H. Lohman, Oy Ajat Ltd.

[121] M. Maiorino et al., *Charge-sharing observations with a CdTe pixel detector irradiated with a ^{57}Co source*, NIM A, 2006, Article in press.

[122] J. Chambron et al., *A Pixellated γ-camera based on CdTe detectors – clinical interests and performances*, NIM A 448, 2000.

[123] R. Franchi et al., *Photon counting X-ray imaging with CdTe pixel detectors based on XPAD2 circuit*, NIM A, 2006, Article in press.

[124] C. Fröjdh et al., *Characterization of a pixellated CdTe detector*, NIM A, 2006, Article in press.

[125] R. Brenner, *Aspects of the DELPHI Vertex Detector and future silicon trackers at LHC*, Report series HU-SEFT R 1996-26, University of Helsinki, Finland, 1996.